Molecular Engineering of Porphyrin-Tapes/Phthalocyanine Heterojunctions for a Highly Sensitive Ammonia Sensor

Giuseppe Bengasi, Rita Meunier-Prest, Kamal Baba, Abhishek Kumar, Anna Lucia Pellegrino, Nicolas D Boscher, Marcel Bouvet

Giuseppe Bengasi, Rita Meunier-Prest, Kamal Baba, Abhishek Kumar, Anna Lucia Pellegrino, Nicolas D. Boscher,* Marcel Bouvet*

Molecular Engineering of Porphyrin-Tapes/Phthalocyanine Heterojunctions for a Highly Sensitive Ammonia Sensor

The development of a new series of organic heterojunctions for ammonia sensing is achieved with a fully dry approach. The top layer is composed of porphyrin tapes synthetized by oCVD. The bottom layer, obtained by sublimation of different phthalocyanines, affects the detecting behavior. The performances obtained place the devices between the best ammonia sensors reported so far.

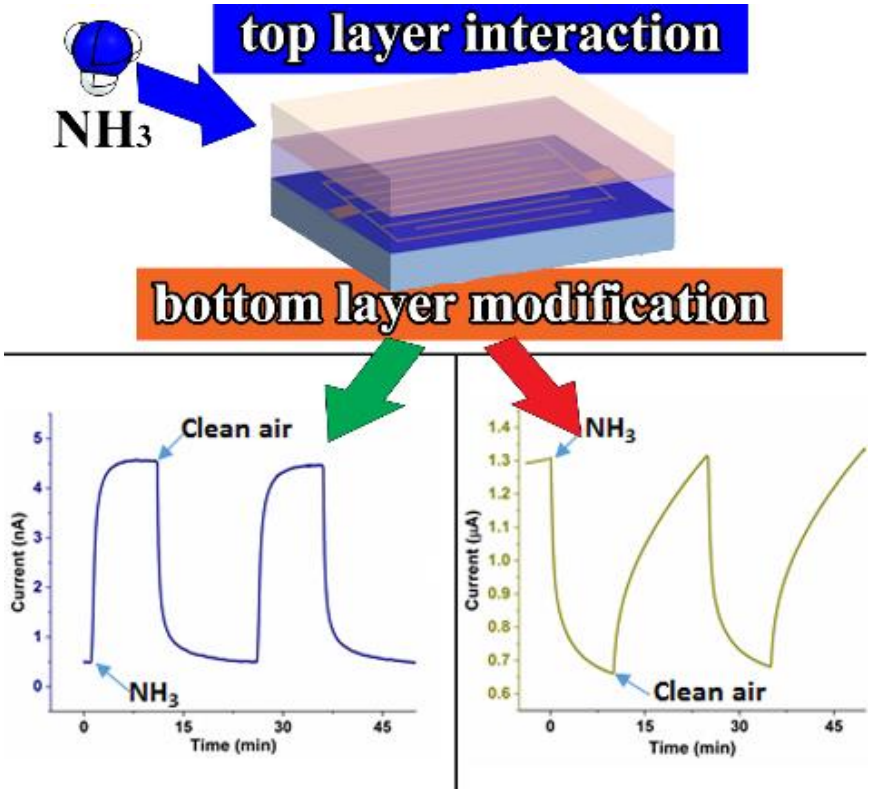

Molecular Engineering of Porphyrin-Tapes/Phthalocyanine Heterojunctions for a Highly Sensitive Ammonia Sensor

Giuseppe Bengasi,[a] Rita Meunier-Prest,[b] Kamal Baba,[a] Abhishek Kumar,[b] Anna Lucia Pellegrino,[a,c] Nicolas D. Boscher,[a,] and Marcel Bouvet[b,*]*

Dr. Giuseppe Bengasi, Dr. Kamal Baba, Dr. Anna Lucia Pellegrino, Dr. Nicolas D. Boscher
Materials Research and Technology Department, Luxembourg Institute of Science and Technology, 5, avenue des hauts-fourneaux, L-4362, Esch-sur-Alzette, Luxembourg
E-mail: nicolas.boscher@list.lu

Dr. Rita Meunier-Prest, Dr. Abhishek Kumar, Prof. Marcel Bouvet
Institut de Chimie Moléculaire de l'Université de Bourgogne (ICMUB), UMR CNRS 6302, Université Bourgogne Franche-Comté, 9 avenue Alain Savary, 21078 Dijon cedex, France.
E-mail: marcel.bouvet@u-bourgogne.fr

Dr. Anna Lucia Pellegrino
Dipartimento di Scienze Chimiche, Università di Catania and INSTM UdR Catania, V.le A. Doria 6, 95125 Catania, Italy.

Keywords: Porphyrins; Phthalocyanines; Heterojunctions; Sensors; Ammonia

Abstract

Modulating the interfacial charge alignments by molecular engineering in an organic heterojunction device is a smart strategy to improve its conductivity, which can be exploited in high performance gas sensors development. Herein, the fabrication of new organic heterojunction devices based on porphyrin tapes and phthalocyanines and their potentiality in ammonia sensing at different relative humidity (rh) are investigated. The devices are built using dry approach relying on oxidative chemical vapor deposition for simultaneous synthesis, doping and deposition of the porphyrin tape layer and physical vapor deposition of phthalocyanine layer. The association of the porphyrin tapes with copper phthalocyanine (CuPc) or its perfluorinated analogue (Cu(F_{16}Pc)) in a bilayer device configuration revealed a non-linear current-voltage characteristics, assigned to the formation of organic heterojunction at the bilayer interface. Cu(F_{16}Pc)-based devices revealed higher response, faster sorption kinetics, stable baseline and less interference from rh fluctuations towards ammonia than CuPc-based devices which are attributed to more conducting interface in the former. Moreover, depending on the porphyrin tape associated, Cu(F_{16}Pc)-based devices exhibited sensitivity

values 6.7 % ppm^{-1} or 0.4 % ppm^{-1} and detection limit of 1 ppm or 228 ppb allowing to obtain among the best NH_3 sensors reported.

1. Introduction

Metalloporphyrinoids (MPor) are fascinating compounds that have been selected by Nature to fulfill a series of important biochemical functions.[1] The coexistence of a conjugated organic macrocyclic structure and a transition metal center provides MPor with numerous properties that fostered their use in catalysis,[2,3] theranostic[4] and non-linear optic.[5] Another application area of MPor is chemosensing,[6] in which interactions with a chemical analyte modifies the physical properties of MPor film that can be transduced into a measurable signal. Based on the nature of signal transductions, MPor based optical, acoustic, magnetic and electrical chemosensors have been developed[7] to detect myriad of species such as redox gases[8], volatile organic compounds[9] and inorganic biochemical species[10]. Particularly, MPor chemosensors based on electrical transductions such as chemiresistors, ChemFet and conductometric sensors have drawn interests exploiting the semiconducting nature of MPor, which can be effectively tuned by adding substituents to its macrocyclic periphery or ligands at the metal center. F. Song and coworkers reported a chemiresistor based on highly ordered film of tetra-amino zinc porphyrin derivative to selectively detect NO_2 at sub-ppm concentration.[11] Elsewhere, self-assembled monolayers of MPor films in ChemFet configuration were used to detect organic vapors and redox gases, exhibiting the strong influence of metal atom on sensors responses.[12,13] However, most of the MPor are poor conducting materials owing to low π-conjugation, limiting the sensors performances. To overcome this limitation, different approaches have been adopted such as forming a composite with more conducting materials like carbon nanotubes,[14,15] conductive polymers[16,17] or metal oxides.[18,19]

An alternative solution to the MPor low conductivity can be the formation of highly conjugated porphyrin polymers to extend the molecular π-system. However, the synthesis of conjugated

porphyrin polymers requires significant synthetic efforts. In 2001, Osuka and co-workers provided a new route towards the easy synthesis of directly fused metalloporphyrins, known as *porphyrin tapes* (**Scheme 1**).[20] Porphyrin tapes possess a series of outstanding properties such as electronic transitions in IR region,[20] increased catalytic activity,[21] two-photon absorption[22] and low conductance attenuation factors.[23,24] The synthesis of porphyrin tapes relies on the oxidative coupling and can be carried out adopting chemical[20] or electrochemical methods.[25,26] However, in case of electrochemical methods, formation of thin films requires the use of conductive substrates, limiting its application in the production of optoelectronic devices. Furthermore, porphyrin tape planar structure favors aggregation and results in poor solubility and unmeltability, thus produces non-uniform thin films, restricting its integration in electronic devices. To achieve sufficient solubility, the use of long and/or bulky substituents able to counterbalance the interaction between the different polymeric chains was proposed.[27,28] However, the presence of substituents on the porphyrin negatively affects its electrical properties inhibiting interaction between the polymeric chains.[29] Very recently, we implemented the oxidative chemical vapor deposition (oCVD) approach for the synthesis of porphyrin tapes.[30] The oCVD approach relies on the simultaneous sublimation of MPor bearing free *meso* and β–positions and an oxidizing agent (e.g. $FeCl_3$) to perform oxidative coupling polymerization directly from the gas phase. Operating from the gas phase also allows circumventing the insolubility and non-meltability of porphyrin tapes, thus yielding *p*-doped porphyrin tapes homogeneous thin films in a single step independent of the substrate.[30]

The oCVD technique was also implemented with different central metal cations,[31] substituents[29,32] and oxidants[33] showing the versatility of this approach for the synthesis of fused porphyrin tapes. Interestingly, we observed that during oCVD, reaction of MPor substituted with aryl groups possessing free *ortho*-positions causes intramolecular dehydrogenative coupling between these *ortho*-positions and nearby β–positions of the porphyrin macrocycle.[29,30,32] As a result of this reaction, the molecule is flattened favoring

interaction between the different polymeric chains and therefore increasing the conductivity of the film.[29] The increased conductivity of phenyl-fused porphyrin tape can be utilized in conductometric gas sensors, which remain an unexplored application area for this material.

Some of us developed an original conductometric gas sensing device based on an organic heterojunction between a poor conducting and a high conducting organic semiconductors, which has shown high sensitivity and selectivity towards redox gases.[34,35] These sensing devices benefit from the organic heterojunction effects in which opposite charges (e^- and h^+) are accumulated at the interface of a bilayer film because of the workfunction difference between the semiconducting layers, enhancing the charge carriers mobility along the interface.[36] In majority of these devices fabricated so far, a poor conducting metal phthalocyanine (MPc) as a sublayer and a high conducting MPc as a top layer were used. A combination of perfluorinated copper phthalocyanine ($Cu(F_{16}Pc)$) and lutetium bis-phthalocyanine ($LuPc_2$) in a bilayer heterojunction configuration exhibited among the best NH_3 sensing performances (detection limit of 140 ppb) as revealed in our recent studies.[37] Octachloro derivatives of different MPc (M: Co, Cu and Zn) were also used as sublayer and showed *n*-type, *p*-type or ambipolar sensing device characteristics depending on the metal atom in MPc under exposure to NH_3 in a wide range of relative humidity (rh).[38] Other than MPc, a few other organic semiconductors such as polyaniline, poly(2,5-dimethoxyaniline),[39,40] carboxylate and fluoro derivatives of perylene[41] as well as inorganic semiconductors like tungsten oxide (WO_3)[42] were also used as sublayer in combination with $LuPc_2$ as top layer to detect NH_3 in the sub-ppm range. Notably, in all these heterojunction sensing devices, top layer remained the same (because majority of MPc have low carrier density) $LuPc_2$ being among a few highly conducting phthalocyanine materials because of its radical nature.[43] Porphyrin tapes represent a suitable alternative to $LuPc_2$ in organic heterojunction gas sensors because their extended π-conjugation imparts high charge carrier concentration. Moreover, its carrier

density can be effectively tuned by changing the conjugation length of the carbon chain or by controlling the spatial orientation of the subunits.[29]

Accordingly, herein we report the fabrication of organic heterojunction gas sensors incorporating MPc or its perfluorinated analogue as a sublayer and porphyrin tapes as a top layer in a bilayer heterostructure configuration (**Scheme 2**) and investigate their potentialities in NH_3 detection in a wide rh range at room temperature. Two different porphyrin tapes, owing different molecular geometry and structure, are investigated as a top layer after their oCVD *in situ* synthesis on a MPc coated substrate (Scheme 1). The microstructure, morphologies, electronic properties and chemical purity of the porphyrin tapes are extensively characterized by XRD, SEM, XPS, mass spectrometry and UV/Vis/NIR spectroscopy. The electrical properties of the devices are studied by recording current-voltage characteristics and the electrical nature of heterojunction interface is evaluated. The ammonia sensing properties of different heterojunction devices are investigated by a fixed duration of exposure and recovery cycles in a dynamic NH_3 concentration and rh. Different sensors analytical parameters, such as sensitivity, repeatability, linear range, limit of detection are finally evaluated.

2. Results and Discussion

2.1. Fabrication of the Chemosensing Devices

The organic heterojunction devices were fabricated by sequential deposition of 50 nm CuPc or its perfluorinated anologue ($Cu(F_{16}Pc)$) by high vacuum sublimation on a glass substrate lithographically patterned with ITO interdigitated electrodes and 40 nm of porphyrin tapes by oCVD (Scheme S1). Two different types of porphyrin tapes, namely pNiDPP and pNiDMP originating from Ni(II) 5,15 (diphenyl) porphyrin (**NiDPP)** and Ni(II) 5,15 (dimesityl) porphyrin (**NiDMP)** monomers, respectively, were investigated as top layer in the heterojunction devices. As illustrated in Scheme 1, S2 and S3, the free ortho-position in the aryl subunit of NiDPP allows an intramolecular cyclization concurrently with the formation of

directly fused porphyrin tapes during oCVD. The cyclization causes a flattening of pNiDPP macrocyclic subunit, resulting in an expanded π–system and improved intermolecular π–π interactions and conductivity.[29] Kojima and co-workers showed that cyclization reaction also lowers the position of LUMO and increases Lewis acidity of the metal center.[44] Thus, pNiDPP exhibits augmented Lewis acidity and an expanded π–system that should facilitate the interaction with reducing gases such as NH_3. On the contrary, NiDMP, because of blocked ortho-position of the aryl moities, is not subjected to intramolecular cyclization, hindering strong intermolecular π–π interactions and thus results in less enhancement in conductivity.[29] Details of the oCVD reactor and oCVD reaction conditions are given in Scheme S1 and Table S1. Thus, four heterojunction devices were realized; namely CuPc/pNiDPP, CuPc/NiDMP, Cu(F_{16}Pc)/pNiDPP and Cu(F_{16}Pc)/pNiDMP. During the oCVD step, glass and silicon substrates were also coated to enable microstructural and elemental characterisation of pNiDPP and pNiDMP thin films.

2.2. Composition, Structure and Morpholgies of the Porphyrin Tapes Thin Films

pNiDPP and pNiDMP fused porphyrin films exhibit a drastic color change, from orange to green/grey, when compared to sNiDPP and sNiDMP reference films prepared from the sole sublimation of the monomers (**Figure 1**). This color change and NIR absorption observed for the porphyrin tapes films (Figure 1), arise from extension of the π-system and are typical to formation of porphyrin tapes.[30] Indeed, the extended π–system in the fused porphyrin raises the energy level of the HOMO facilitating electronic transition and consequently absorption in the NIR region.[20] Due to the cyclization reactions, the spectrum of pNiDPP shows an intense broadening while pNiDMP, in which no cyclization takes place, exhibits well defined absorption bands associated with the formation of doubly and triply linked porphyrin tapes.[29] The occurrence of the oxidative polymerization reaction during oCVD is confirmed by LDI-HRMS analysis on the porphyrin tapes film (**Figure S1**), showing the peaks corresponding to

the formation of fused porphyrin oligomers. The mass spectra also exhibit a family of peaks distribution related to the exchange of hydrogen atoms with chlorine, which is attributed to the presence of Cl_2 produced during the sublimation of $FeCl_3$.[33] The spectrum also confirms occurrence of the cyclization reaction in pNiDPP showing loss of more than 6H atoms in the dimeric region (Figure 1c). Particularly, every coupling reaction (i.e. singly/doubly/triply linked units and/or cyclization) causes the loss of hydrogen atom pairs (-2H) (Scheme S2 and S3). While the most intense peaks in pNiDMP dimeric region correspond to the formation of doubly and triply linked porphyrin tapes **(**$NiDMP_2$ -4H and -6H species in Figure 1c), pNiDPP exhibits signals with high intensity corresponding to more unsaturated species ($NiDPP_2$ -8H, $NiDPP_2$ -10H and $NiDPP_2$ -12H) due to the occurrence of cyclization reaction (Scheme S2 and S3). Species associated to the loss of more than 6H were observed at lower intensity also in pNiDMP mass spectrum (Figure 1d). We recently showed that the formation of additional unsaturated species also takes place for pNiDMP, probably due to surface reactions catalyzed by iron species.[29] Although we didn't identify the exact nature of this species, we observed a marginal abundance of such molecules during the oCVD of pNiDMP.[29] LDI-HRMS also shows, in both samples, that the presence of demetalated porphyrins is negligible, confirming the high stability of Ni(II) cation in the porphyrin tapes.

In addition, the relative atomic compositions, obtained by XPS of pNiDMP and pNiDPP thin films are close to the theoretical ones of their respective monomers (Table S2). The binding energy of Ni 2p peak in all samples is constant at 855.4 eV, confirming the retention of the nickel center during the oxidative coupling of porphyrin during oCVD (**Figure S2**). Analysis of the valence band XPS spectra of porphyrin tapes and their respective monomers indicates the shifting of valence bands maximum (VBM) towards lower binding energy after polymerization (**Figure 2**). It implies that HOMO level shifts upward after polymerization, narrowing the band gap of the porphyrin tapes from their respective monomer. Notably, pNiDPP spectrum depicts lower VBM value (1.5 eV) compared to pNiDMP (1.93 eV), which

also translates into higher HOMO energy of pNiDPP, which can be attributed to the intramolecular cyclization reaction during oCVD process extending the conjugation length.

Thin films morphologies studied by FE-SEM (**Figure 3b and 3c**) revealed a slightly different morphology for the two porphyrin tapes. In fact, pNiDMP displays a more ruffled and corrugated surface that may be ascribed to steric hindrance associated with mesityl groups causing less regular arrangements of the polymer chains (see below). pNiDPP film exhibits a more porous morphology that could be attributed to the cyclization reaction. Particularly, the cyclization reaction involves the production of gaseous by-products that bubbles out from the film causing the formation of pores.[45] Lower magnification SEM images of the both materials are shown in **Figure S3** and **S4** depicting a compact surface and the presence of residual oxidant $FeCl_3$ used in the CVD process.

To further understand the organizations in pNiDMP and pNiDPP thin films, in depth structural characterization was made by XRD. The XRD patterns display several peaks, pointing to the formation of an ordered distribution of the porphyrin tapes (Figure 3 a). All the peak values are summarized in Table S3 and for each of them the corresponding plane distance was derived. Notably, both materials have polycrystalline organization. However, pNiDPP film presents more numerous and intense signals, thus suggesting higher crystalline degree.

The extrapolated distances, ranging between 5.55 Å and 2.31 Å, may be associated with parallel orientations of the conjugated porphyrins tapes. This assumption is in agreement with our DFT study on a model composed of two monomeric units showing an estimated distance between parallel porphyrin units around 3.3 Å.[29] We expect that moving from monomer model into porphyrin tapes would lead to increased interplanar distances due to the steric hindrance.[46] Accordingly, X-ray single crystal structures of the fused dimers and trimers obtained for 3,5-di-tert-butylphenyl-substituted and pentafluorophenyl-substituted Zn and Ni porphyrins showed various interplanar distances between 3.75 Å and 9.60 Å for the bigger substituent units.[46] On the contrary, the interplanar distances should be reduced by the cyclization reaction in

NiDPP due to planarization of the molecule. Indeed, only pNiDPP film exhibits signals related to interplanar distances smaller than 3 Å. Furthermore, cyclization and the consequent planarization of the molecule could account for the higher crystallinity observed for pNiDPP film compared to pNiDMP. Second order reflections (Table S3) are also likely contributing to the diffraction patterns. In a similar fashion, PEDOT films obtained by oCVD shows 0k0 reflections XRD pattern at 26°, indicating the presence of parallel orientation of the polymeric chains.[47] The parallel orientation of the porphyrin tapes is also corroborated by the FE-SEM (Figure S3 and S4) images of the films showing in both cases flat and smooth surfaces. In order to exclude contributions of residual monomers in the XRD patterns, we also acquired XRD patterns of the monomer powders and films formed by sublimation of the monomer.

Comparison between NiDMP monomer powder and pNiDMP film XRD patterns does not show any overlap of the peaks (**Figure S5**) allowing to exclude any contribution of the monomer into the XRD pattern of the oCVD film. On the contrary, NiDPP monomer powder and the pNiDPP film's XRD patterns present both the peaks at 15.96°, 20.70° and 22.35°(**Figure S6**). We also acquired XRD pattern of sublimated NiDPP (sNiDPP) film deposited under the same operative condition as of pNiDPP. The comparison between the XRD patterns of NiDPP powder, sNiDPP and pNiDPP films is reported in **Figure S7**. The XRD pattern of sNiDPP film shows a unique peak at 5.15°, which is also present in NiDPP powder pattern but not in pNiDPP film one. This observation excludes any contribution of residual monomer to the XRD pattern of pNiDPP. The peak at 5.15° corresponds to 17.14 Å plane distance. This value can be rationalized hypothesizing a perpendicular packing of the monomeric porphyrins on the substrate. The assumption is further validated by the DFT calculations, showing distance between the two phenyl rings in NiDPP molecule around 17.28 Å[32] which is in agreement with a perpendicular stacking of the porphyrins through the planes. Finally, the contribution of Fe-Cl crystalline phase has been also excluded considering the diffraction files PDF00-001-1106 ($FeCl_2$), and 04-005-5140 ($FeCl_3$).

2.3. Electrical Properties of the Heterojunction Devices

Electrical properties of pNiDPP and pNiDMP porphyrin tapes film deposited onto chips patterned with interdigitated electrodes were investigated. The recorded current-voltage (I(V)) characteristics revealed ohmic behavior for both porphyrin tapes films, confirming a resistor like properties. The conductivity values obtained for pNiDPP and pNiDMP are 1×10^{-4} $S\cdot cm^{-1}$ and 1×10^{-8} $S\cdot cm^{-1}$, respectively. The higher conductivity of pNiDPP film is attributed to the intramolecular cyclization leading to molecular flattening that intensify the π–π interactions and reduces the intermolecular distances. **Figure 4** depicts the I(V) curves of 4 different heterojunction devices based on a bilayer of porphyrin tape on phthalocyanine, exhibiting a non-linear but symmetric characteristics (except CuPc/pNiDMP device).

The current values obtained at a bias voltage of +10 V are 5.5×10^{-6} A, 7.5×10^{-7} A and 5.5×10^{-9} A for CuPc/pNiDPP, Cu(F_{16}Pc)/pNiDPP and Cu(F_{16}Pc)/pNiDMP devices, respectively, while CuPc/pNiDMP revealed unstable and huge hysteresis in the output current on a reverse voltage sweep. It is evident that heterojunction devices' current changes as a function of top layer and sublayer. Unstable I(V) curve with high hysteresis for CuPc/pNiDMP device is attributed to the relatively larger amount of residual Fe^{3+} and Cl^- ions in pNiDMP layer also confirmed by its XPS elemental analysis. Nonetheless, heterojunction device having the same porphyrin tape, but with Cu(F_{16}Pc) as sublayer showed a highly symmetrical, stable and less hysteresis in its current, indicating that charges alignment at the bilayer interface plays a crucial role. The interfacial charges distribution is determined by the semiconducting polarity, workfunction and the carrier concentration of each material in the bilayer.[36] For Cu(F_{16}Pc) based devices, because of the very high workfunction of the sublayer and its *n*-type semiconducting behavior, e^- and h^+ are accumulated at the interface and an accumulation heterojunction is formed (**Figure 5a**). On the contrary, in CuPc based devices, owing to its *p*-type behavior and low workfunction, holes are accumulated in the sublayer and depleted in the top layer near the interface, and the

heterojunction so developed is of the type hole accumulation/depletion (Figure 5b). It is worth mentioning that in Cu(F_{16}Pc) based heterojunctions, mobile carriers (e^- and h^+) are accumulated turning the interface highly conducting. On the other hand, CuPc based heterojunctions have only half of the interface filled with free carrier (h^+) while the other half is occupied by immobile charges. Thus, instability and large hysteresis in the CuPc/pNiDMP device results from large accumulation of residual Cl^- ions in the top layer near the interface. Because of the opposite charges alignment at the heterojunction interface, an energy barrier is developed which can be quantified by measuring the x-intercept of the tangent to I(V) curves at high bias voltage. The apparent energy barrier (U_{th}) estimated for CuPc/pNiDPP, Cu(F_{16}Pc)/pNiDPP and Cu(F_{16}Pc)/pNiDMP devices are 0.72 V, 1.82 V and 1.91 V, highlighting strong effect of the sublayer on the heterojunction device electrical properties. The U_{th} of CuPc/pNiDMP could not be calculated because of non-reproducibility of its I(V) curves.

2.4. Ammonia Sensing Properties of the Heterojunction Devices

The implication of different interfacial charges alignments in heterojunction devices were investigated on their ammonia sensing properties, performed in a dynamic mode by alternate exposure under 90 ppm NH_3 and a recovery under clean air devoid of NH_3 for an interval of 10 and 15 minutes, respectively. A current decrease during exposure and an increase under recovery cycle were observed (**Figure 6a and 6b**) for CuPc based heterojunctions, highlighting the *p*-type semiconducting polarity of the device considering the electron donating nature of ammonia. The relative responses (RR) (calculated by equation 1) for different exposure cycles were -24 % and -48 % and response time ($t_{90\%}$) were 3.9 min and 4.3 min for CuPc/pNiDPP and CuPc/pNiDMP heterojunctions, respectively, indicating the influence of top porphyrin tapes film on the sensors response. Moreover, a significant drift in CuPc/pNiDPP device baseline current is also noticeable. However, similar recovery time ($t_{90\%}$) (12 min) were estimated for both devices.

$$RR\ (\%) = \frac{I_{NH3} - I_0}{I_0} \times 100 \qquad (1)$$

Interestingly, the heterojunction devices based on Cu(F_{16}Pc) sublayers show a current increase under NH_3 exposure and current decrease during clean air recovery step (Figure 6c and 6d), highlighting *n*-type semiconducting polarity of the device and key role played by the sublayer on the transport properties of the heterojunction devices. These devices showed a very stable baseline, higher RR and faster response and recovery times from those based on CuPc sublayer (Table S4). Moreover, the strong influence of different porphyrin tapes top layer is also exemplified, such that Cu(F_{16}Pc)/pNiDMP exhibits much higher RR (788 %), faster response and recovery time than Cu(F_{16}Pc)/pNiDPP device. However, it is worth mentioning that high RR of Cu(F_{16}Pc)/pNiDMP device is partly because of very low range of baseline current (I_0). The opposite trend in the responses towards NH_3 and faster kinetics in exposure and recovery cycles can be attributed to the different interfacial charges distribution in CuPc and Cu(F_{16}Pc) based devices (Figure 5). Ammonia being an electron donating gas, acts as a chemical dopant of e^- in the sensor top surface. Upon exposure, NH_3 neutralizes h^+ in the *p*-type top layer, disturbing e^- and h^+ accumulation equilibrium at the interface, concurrently decreasing the workfunction of the top layer, consequently top layer injects e^- in the sublayer enhancing carrier density in the sublayer. The heterojunction device current is determined by free carriers concentration in the sublayer because electrodes are embedded there. Accordingly, current increase is noticed during NH_3 exposure and decrease under recovery cycles. Faster kinetics of Cu(F_{16}Pc) based sensors' responses and recovery can be also correlated with the nature of charges distribution at the interface. Notably, in the accumulation heterojunction (Figure 5a), free carriers are accumulated at the interface, turning it highly conducting. Since, free carriers (e^- and h^+) are highly mobile, any external doping (such as e^- from ammonia) is quickly

delocalized and interface charge redistribution takes place in a short time. That is why, relatively shorter response and recovery time are obtained for Cu(F_{16}Pc) based devices.

It is obvious from the previous discussion that heterojunction devices based on Cu(F_{16}Pc) sublayer are better ammonia sensors at a fixed concentration, so further sensing characteristics of the devices towards variable ammonia concentrations and under the humid atmosphere were performed by employing short exposure and recovery cycles of 1 and 4 minutes, respectively, in a concentration range of 1 to 50 ppm of ammonia. The current variations of Cu(F_{16}Pc)/pNiDPP and Cu(F_{16}Pc)/pNiDMP devices submitted to different concentrations of ammonia in a range of 10 to 50 ppm, increasing in a step of 5 ppm and at a rh of 40 % are shown in **Figure 7**. The current increase associated with each exposure and decrease during the recovery periods are clearly noticeable for both the devices. Additionally, reponses are highly repeatable because similar variations in the current were obtained for 5 exposure-recovery cycles recorded at each concentration. At a first glance, Cu(F_{16}Pc)/pNiDMP device appears a better NH_3 sensor highlighted by a linear enhancement in the device current with increasing concentration, while a saturation in the current increase is noticeable at higher concentration in Cu(F_{16}Pc)/pNiDPP device. However, it is worth noting that Cu(F_{16}Pc)/pNiDMP device requires higher bias voltage (5 V) to produce a stable response compared to lower bias voltage (2 V) required for Cu(F_{16}Pc)/pNiDPP device. Responses towards ammonia were also studied at lower concentrations in a range of 1–9 ppm (**Figure S8**) for both the devices. A calibration curve depicting sensors relative response as a function of ammonia concentration is shown for both the devices in Figure 7c and 7d. It is obvious from these calibration curves that Cu(F_{16}Pc)/pNiDMP sensor response is linear in the studied concentration range of 1–50 ppm, correlated through the equation (2) with correlation coefficient 0.998 (Figure 7c).

$$RR_{NH3} = (6.67 \times C_{NH3}) - 10.10 \qquad (2)$$

As expected, similar calibration plot of the device based on Cu(F_{16}Pc)/pNiDPP shows a non-linear behavior in the studied ammonia concentration range, which RR in low concentration range is decribed by the linear equation (3) with a correlation cofficient 0.996.

$$RR_{NH3} = (0.403 \times C_{NH3}) \quad (3)$$

RR of Cu(F_{16}Pc)/pNiDMP sensor is up to 25 times higher than Cu(F_{16}Pc)/pNiDPP as evident from the calibration plots, but mainly because of very low baseline current. Based on the calibration plots, sensors analytical parameters were determined. The slope of linear correlation of the calibration plots corresponds to sensitivity of the sensors, which is 6.66 % ppm^{-1} and 0.403 % ppm^{-1} for Cu(F_{16}Pc)/pNiDMP and Cu(F_{16}Pc)/pNiDPP devices, respectively. Such a high sensitivity of the device led us to obtain a limit of detection of ca. 1 ppm and 228 ppb for Cu(F_{16}Pc)/pNiDMP and Cu(F_{16}Pc)/pNiDPP devices, respectively, which are below the mandated international guidelines of ammonia exposure, thus making the devices suitable for commercial applications. The ammonia sensitivity was also investigated for CuPc sublayer based devices (**Figure S9**). They reveal huge drift in the baseline current coupled with low sensitivity values (S = -0.04 ppm^{-1} and -0.19 ppm^{-1} in the studied concentration range for CuPc/pNiDPP and CuPc/pNiDMP, respectively) and non-linear variations in the responses, making them unsuitable for ammonia sensing.

2.5. Humidity Effects on Ammonia Sensing

Humidity remains an important criterion to evaluate the performance of ammonia sensors considering the detection of ammonia in real environmental conditions. Accordingly, Cu(F_{16}Pc)/pNiDMP and Cu(F_{16}Pc)/pNiDPP devices' current variations under repeated exposure to 20 ppm of ammonia and recovery under clean air were investigated in variable rh in a range of 30–60 %. The sensors behavior as shown in **Figure 8** exhibited a reversible response at a constant rh value and an enhancement in the response with increasing rh values,

which are expected taking into account the electron donating nature of water molecules. Notably, RR of Cu(F_{16}Pc)/pNiDMP device experiences a larger variation from 4 % to 10 % compared to 6.5 % to 8.5 % noted for Cu(F_{16}Pc)/pNiDPP (Figure 8c), which makes later as a better NH_3 sensors in terms of stability under rh fluctuation. On the other hand, CuPc based devices were highly unstable and less sensitive in the similar rh range, exhibiting huge drift in the device baseline as well as very high interference in NH_3 responses by rh (**Figure S10**).

The NH_3 sensing performances such as RR, sensitivity, detection limit, stability of the present device are compared with the other heterojunction devices developed previously in our group and other NH_3 sensors reported in literature. As summarized in **Table S5**, Cu(F_{16}Pc)/pNiDPP performances are among the best NH_3 sensors demonstrated by higher RR, sensitivity and lower detection limit from majority of the previously reported such sensors. Moreover, the present study also justifies the use of porphyrin tapes as a suitable alternative to $LuPc_2$ in organic heterojunction devices to obtain a highly sensitive redox gas detection platform.

3. Conclusions

In conclusion, we undeniably demonstrated the potential of a new series of porphyrin tape/metal phthalocyanine heterojunction devices for the conductometric detection of NH_3. The devices own performances suitable for commercial application and are synthetized relying on easily up-scalable solvent-free methods. Two different porphyrin tapes, pNiDPP and pNiDMP, synthetized by oCVD were investigated as top layer. In pNiDPP, the free -*ortho* position on the phenyl substituents, allows a ring fusion affecting the porphyrin's π-system, the microstructural organization of the polymer and the conductivity of the film. Heterojunction devices incorporating porphyrin tape and phthalocyanine exhibited non-linear I(V) characteristics attributed to formation of an energy barrier at the heterojunction interface because of workfunction difference between the porphyrin tape and the phthalocyanine. In fact, CuPc based devices formed accumulation-depletion heterojunction while Cu(F_{16}Pc) based

devices formed accumulation heterojunction. Accordingly, NH_3 sensing properties of the device is determined as CuPc based devices experienced current decrease while Cu(F_{16}Pc) based devices showed current increase under NH_3 exposure and vice versa for the recovery under clean air, thus exhibiting *p*-type and *n*-type semiconducting polarity of these devices. Sensing properties of Cu(F_{16}Pc) based devices is superior to CuPc based ones manifested by larger RR, faster adsorption/desorption kinetics and stable response for NH_3 exposure and recovery periods. Moreover, RR of Cu(F_{16}Pc) based devices are less affected by the variations in rh contrary to CuPc based devices which response become highly unstable and huge baseline drift is noticed under variable rh environment. Among different devices, Cu(F_{16}Pc)/pNiDPP demonstrated minimum interference and highest stability at different rh levels and also showed a detection limit down to 228 ppb, which makes it among the best ammonia sensors and can be applied to detect NH_3 in real conditions. In addition, the present work validates the successful integration of porphyrin tapes in organic heterojunction devices which will open a large window of new heterojunction devices development in future. These heterojunction sensing devices will be further investigated for a series of oxidizing and reducing gases and in depth sensors performances will be evaluated.

4. Experimental Section

4.1. Chemicals

CuPc was purchased from Sigma Aldrich and Cu(F_{16}Pc) was synthesized according to a previously described method.[48] NiDPP and NiDMP were purchased from PorphyChem and used without further purifications. Iron(III) chloride (97 %), purchased from Sigma-Aldrich, was used as oxidant without further purifications.

4.2. Oxidative Chemical Vapor Deposition

The pNiDMP and pNiDPP thin films were prepared in a custom built oCVD reactor (details in Figure S1) using commercially available metalloporphyrins (NiDMP and NiDPP). (see

Table S1 for detailed deposition conditions). The reference NiDMP and NiDPP thin films were prepared by simple sublimation in the same oCVD reactor. The samples prepared for the XRD analysis were obtained increasing the deposition time to 60 minutes.

4.3. Thin Film Characterization

The thickness of the porphyrin tapes thin films was evaluated by a spectroscopic ellipsometer FS-1. The spectrometric ellipsometry measurements were acquired at a single angle of 65° using four different wavelengths, that is, 465, 525, 590 and 635 nm, and the data were fitted to a Cauchy model. The optical absorbance of the thin films deposited on glass substrate was measured in the range of 250–2000 nm with a UV/Vis/NIR spectrophotometer (PerkinElmer, Lambda 950) with a 150 mm-diameter integrating sphere. LDI-HRMS analyses were performed with an LTQ/Orbitrap Elite Hybrid Linear Ion Trap-Orbitrap Mass Spectrometer from Thermo Scientific coupled with an AP-LDI (ng) UHR source from MassTech Inc with a 355 nm Nd:YAG laser. The thin films were directly probed without any matrix deposition by the laser following a spiral motion during 30 seconds per sample. XPS analyses were performed on a Kratos Axis Ultra DLD instrument using a monochromatic Al Kα X-ray source ($h\upsilon$ = 1486.6 eV) at a power of 105 W. Charge calibration was accomplished by fixing the binding energy of the main carbon (C 1s) contribution to 285.0 eV, associated to the pyrrole rings forming the porphyrin macrocycles. Film surface morphology was investigated using the field emission scanning electron microscope, ZEISS Supra 55 VP. Film structure was analyzed by X-ray diffraction (XRD) in grazing incidence mode (0.5°) using a Bruker D8, equipped with a rotating anode of Cu Kα radiation (λ = 1.54 Å) operating at 20 kV and 40 mA.

4.4. Devices and Electrical Measurements

The lateral thin-film conductivity was evaluated from a simple linear fit approximating all the samples to ohmic materials from two-point current-voltage scans recorded on chips patterned with interdigitated electrodes. The measurements were performed at room temperature and

under ambient atmosphere and the geometry of the channel was 2.5 μm (length), 10 mm (total width), 40 nm (height). The data were recorded using a Keithley (2401) sourcemeter by sweeping the voltage from –4 V to 4 V and back (hysteresis scan) at a scan rate of 500 mV s^{-1}. Chemosensing electrical measurements were carried out with Indium Tin Oxide (ITO) interdigitated electrodes (IDEs), separated by 75 μm and lithographically patterned on a 1 x 1 cm^2 glass substrate. Thin films of the phthalocyanines were prepared by sublimation under secondary vacuum (ca. 10^{-6} mbar) in UNIVEX 250 thermal evaporator (Oerlikon, Germany), by heating in a temperature range of 420-480°C. The deposition was performed at a rate of 1 Å s^{-1} determined by a Quartz Crystal Microbalance positioned close to the substrate and finally 50 nm of films were obtained for each of the phthalocyanine.

Ammonia sensing at different relative humidity (rh) was performed at a custom built automated workstation[41] connected with commercial cylinders of ammonia (985 ppm and 98 ppm in synthetic air) and synthetic air (purchased from Air Liquide, France) and interfaced with a Keithley electrometer. The volume of the sensor testing chamber was 8 cm^3 and the total flow in the fluidic channel was in the range 0.5-0.55 $NL.min^{-1}$, depending on ammonia concentration. The sensing experiments were performed in a dynamic mode by alternatively passing ammonia and synthetic air at a fixed period in the test chamber and simultaneously recording change in the current. All the aformentioned measurements were performed at room temperature

Acknowledgments

The authors gratefully acknowledge the financial support of the Luxembourg National Research Fund (FNR.lu) through the POLYPORPH project (C15-MS-10340560) and the *Agence Nationale de la Recherche (ANR)* for funding through the OUTSMART project (ANR-2015-CE39-0004-03). Financial support from the European Union (FEDER), *Conseil Régional de Bourgogne Franche-Comté* and the *Conseil Régional de Bourgogne* through the FABER and

the PARI SMT 08 and CDEA programs is gratefully acknowledged. We also thank the *Conseil Régional de Bourgogne for providing funding* through the CPER program. This work was also partly supported by the European Union through the PO FEDER-FSE Bourgogne 2014/2020 via the CoMICS program (Chemistry of Molecular Interactions: Catalysis & Sensors). Dr. G. Frache, D. El Assad, Dr. J. Guillot and J.-L. Biagi from LIST and Prof. G. Malandrino from the University of Catania are acknowledged for the HRMS, XPS and SEM measurements and insightful discussions.

References

[1] T. L. Poulos, *Chem. Rev.*, **2014**, *114*, 3919–3962.

[2] K. Ladomenou, M. Natali, E. Iengo, G. Charalampidis, F. Scandola, A. G. Coutsolelos, *Coord. Chem. Rev.*, **2015**, *304–305*, 38–54.

[3] K. Rybicka-Jasińska, W. Shan, K. Zawada, K. M. Kadish, D. Gryko, *J. Am. Chem. Soc.*, **2016**, *138*, 15451–15458.

[4] M. Ethirajan, Y. Chen, P. Joshi, R. K. Pandey, *Chem. Soc. Rev.*, **2011**, *40*, 340–362.

[5] M. O. Senge, M. Fazekas, E. G. A. Notaras, W. J. Blau, M. Zawadzka, O. B. Locos, E. M. Ni Mhuircheartaigh, *Adv. Mater.*, **2007**, *19*, 2737–2774.

[6] R. Paolesse, S. Nardis, D. Monti, M. Stefanelli, C. Di Natale, *Chem. Rev.*, **2017**, *117*, 2517–2583.

[7] S. Ishihara, J. Labuta, W. Van Rossom, D. Ishikawa, K. Minami, J. P. Hill, K. Ariga, *Phys. Chem. Chem. Phys.*, **2014**, *16*, 9713–9746.

[8] S. Yuvaraja, S. G. Surya, V. Chernikova, M. T. Vijjapu, O. Shekhah, P. M. Bhatt, S. Chandra, M. Eddaoudi, K. N. Salama, *ACS Appl. Mater. Interfaces*, **2020**, *12*, 18748–18760.

[9] A. D'Amico, C. Di Natale, R. Paolesse, A. Macagnano, A. Mantini, *Sens. Actuators B Chem*, **2000**, *65*, 209–215.

[10] D. J. Dobson, S. Saini, *Anal. Chem.*, **1997**, *69*, 3532–3538.

[11] F. Song, P. Ma, C. Chen, J. Jia, Y. Wang, P. Zhu, *J. Colloid Interface Sci.*, **2016**, *474*, 51–57.

[12] M. Andersson, M. Holmberg, I. Lundström, A. Lloyd-Spetz, P. Mårtensson, R. Paolesse, C. Falconi, E. Proietti, C. Di Natale, A. D'Amico, *Sens. Actuators B Chem*,

2001, *77*, 567–571.

[13] C. Gu, L. Sun, T. Zhang, T. Li, *Thin Solid Films*, **1996**, *284–285*, 863–865.

[14] M. Penza, R. Rossi, M. Alvisi, M. A. Signore, E. Serra, R. Paolesse, A. D'Amico, C. Di Natale, *Sens. Actuators B Chem*, **2010**, *144*, 387–394.

[15] M. Penza, M. Alvisi, R. Rossi, E. Serra, R. Paolesse, A. D'Amico, C. Di Natale, *Nanotechnology*, **2011**, *22*, 125502.

[16] C. H. A. Esteves, B. A. Iglesias, R. W. C. Li, T. Ogawa, K. Araki, J. Gruber, *Sens. Actuators B Chem*, **2014**, *193*, 136–141.

[17] A. M. Andringa, M. J. Spijkman, E. C. P. Smits, S. G. J. Mathijssen, P. A. va. Hal, S. Setayesh, N. P. Willard, O. V. Borshchev, S. A. Ponomarenko, P. W. M. Blom, D. M. de Leeuw, *Org. Electron.*, **2010**, *11*, 895–898.

[18] S. Nardis, D. Monti, C. Di Natale, A. D'Amico, P. Siciliano, A. Forleo, M. Epifani, A. Taurino, R. Rella, R. Paolesse, *Sens. Actuators B Chem*, **2004**, *103*, 339–343.

[19] E. Callone, G. Carturan, M. Ischia, M. Epifani, A. Forleo, P. Siciliano, R. Paolesse, *Inorganica Chim. Acta*, **2008**, *361*, 79–85.

[20] A. Tsuda, A. Osuka, *Science*, **2001**, *293*, 79–82.

[21] D. Khusnutdinova, B. L. Wadsworth, M. Flores, A. M. Beiler, E. A. Reyes Cruz, Y. Zenkov, G. F. Moore, *ACS Catal.*, **2018**, *8*, 9888–9898.

[22] D. Y. Kim, T. K. Ahn, J. H. Kwon, D. Kim, T. Ikeue, N. Aratani, A. Osuka, M. Shigeiwa, S. Maeda, *J. Phys. Chem. A*, **2005**, *109*, 2996–2999.

[23] G. Sedghi, L. J. Esdaile, H. L. Anderson, S. Martin, D. Bethell, S. J. Higgins, R. J. Nichols, *Adv. Mater.*, **2012**, *24*, 653–657.

[24] N. Algethami, H. Sadeghi, S. Sangtarash, C. J. Lambert, *Nano Lett.*, **2018**, *18*, 4482–4486.

[25] T. Ogawa, Y. Nishimoto, N. Yoshida, N. Ono, A. Osuka, *Angew. Chemie Int. Ed.*, **1999**, *38*, 176–179.

[26] M. A. Vorotyntsev, D. V. Konev, C. H. Devillers, I. Bezverkhyy, O. Heintz, *Electrochim. Acta*, **2011**, *56*, 3436–3442.

[27] N. Aratani, A. Takagi, Y. Yanagawa, T. Matsumoto, T. Kawai, Z. S. Yoon, D. Kim, A. Osuka, *Chem. Eur. J*, **2005**, *11*, 3389–3404.

[28] T. Ikeda, J. M. Lintuluoto, N. Aratani, S. Y. Zin, D. Kim, A. Osuka, *Eur. J. Org. Chem.*, **2006**, 3193–3204.

[29] G. Bengasi, J. S. Desport, K. Baba, J. P. Cosas Fernandes, O. De Castro, K. Heinze, N. D. Boscher, *RSC Adv.*, **2020**, *10*, 7048–7057.

[30] G. Bengasi, K. Baba, G. Frache, J. Desport, P. Gratia, K. Heinze, N. D. Boscher, *Angew. Chemie Int. Ed.*, **2019**, *58*, 2103–2108.

[31] G. Bengasi, L. Quétu, K. Baba, A. Ost, J. P. Cosas Fernandes, P. Grysan, K. Heinze, N. D. Boscher, *Eur. J. Inorg. Chem.*, **2020**, *2020*, 1938–1945.

[32] G. Bengasi, K. Baba, O. Back, G. Frache, K. Heinze, N. D. Boscher, *Chem. Eur. J.*, **2019**, *25*, 8313–8320.

[33] K. Baba, G. Bengasi, D. El Assad, P. Grysan, E. Lentzen, K. Heinze, G. Frache, N. D. Boscher, *Eur. J. Org. Chem.*, **2019**, *2019*, 2368–2375.

[34] V. Parra, J. Brunet, A. Pauly, M. Bouvet, *Analyst*, **2009**, *134*, 1776–1778.

[35] M. Bouvet, V. Parra, *Semiconductor Tranducer and Its Use in a Sensor for Detecting Electron-Donor or Electron-Acceptor Species*, **2013**, U.S. Patent 8,450,725.

[36] H. Wang, D. Yan, *NPG Asia Mater.*, **2010**, *2*, 69–78.

[37] M. Mateos, R. Meunier-Prest, J. M. Suisse, M. Bouvet, *Sens. Actuators B Chem*, **2019**, *299*, 126968.

[38] S. Ouedraogo, R. Meunier-Prest, A. Kumar, M. Bayo-Bangoura, M. Bouvet, *ACS Sens.*, **2020**, *5*, 1849–1857.

[39] M. Mateos, M.-D. Tchangaï, R. Meunier-Prest, O. Heintz, F. Herbst, J.-M. Suisse, M. Bouvet, *ACS Sens.*, **2019**, *4*, 740–747.

[40] M. Mateos, R. Meunier-Prest, O. Heintz, F. Herbst, J. M. Suisse, M. Bouvet, *ACS Appl. Mater. Interfaces*, **2018**, *10*, 19974–19986.

[41] P. Gaudillat, A. Wannebroucq, J. M. Suisse, M. Bouvet, *Sens. Actuators B Chem*, **2016**, *222*, 910–917.

[42] M. Bouvet, M. Mateos, A. Wannebroucq, E. Navarrete, E. Llobet, *J. Mater. Chem. C*, **2019**, *7*, 6448–6455.

[43] M. Bouvet, Radical Phthalocyanines and Intrinsic Semiconduction in *The Porphyrin Handbook*, (Eds.: K.M. Kadish, K.M. Smith, R. Guilard), Academic Press: Amsterdam, **2003**, pp. 37–103.

[44] Y. Saegusa, T. Ishizuka, K. Komamura, S. Shimizu, H. Kotani, N. Kobayashi, T. Kojima, *Phys. Chem. Chem. Phys.*, **2015**, *17*, 15001–15011.

[45] K. Baba, G. Bengasi, F. Loyer, J. P. Cosas Fernandes, D. El Assad, O. De Castro, N. D. Boscher, *ACS Appl. Mater. Interfaces*, **2020**, DOI 10.1021/acsami.0c09630.

[46] T. Tanaka, B. S. Lee, N. Aratani, M. C. Yoon, D. Kim, A. Osuka, *Chem. Eur. J*, **2011**, *17*, 14400–14412.

[47] A. Ugur, F. Katmis, M. Li, L. Wu, Y. Zhu, K. K. Varanasi, K. K. Gleason, *Adv. Mater.*,

2015, *27*, 4604–4610.

[48] J. M. Birchall, R. N. Haszeldine, J. O. Morley, *J. Chem. Soc. C*, **1970**, 2667–2672.

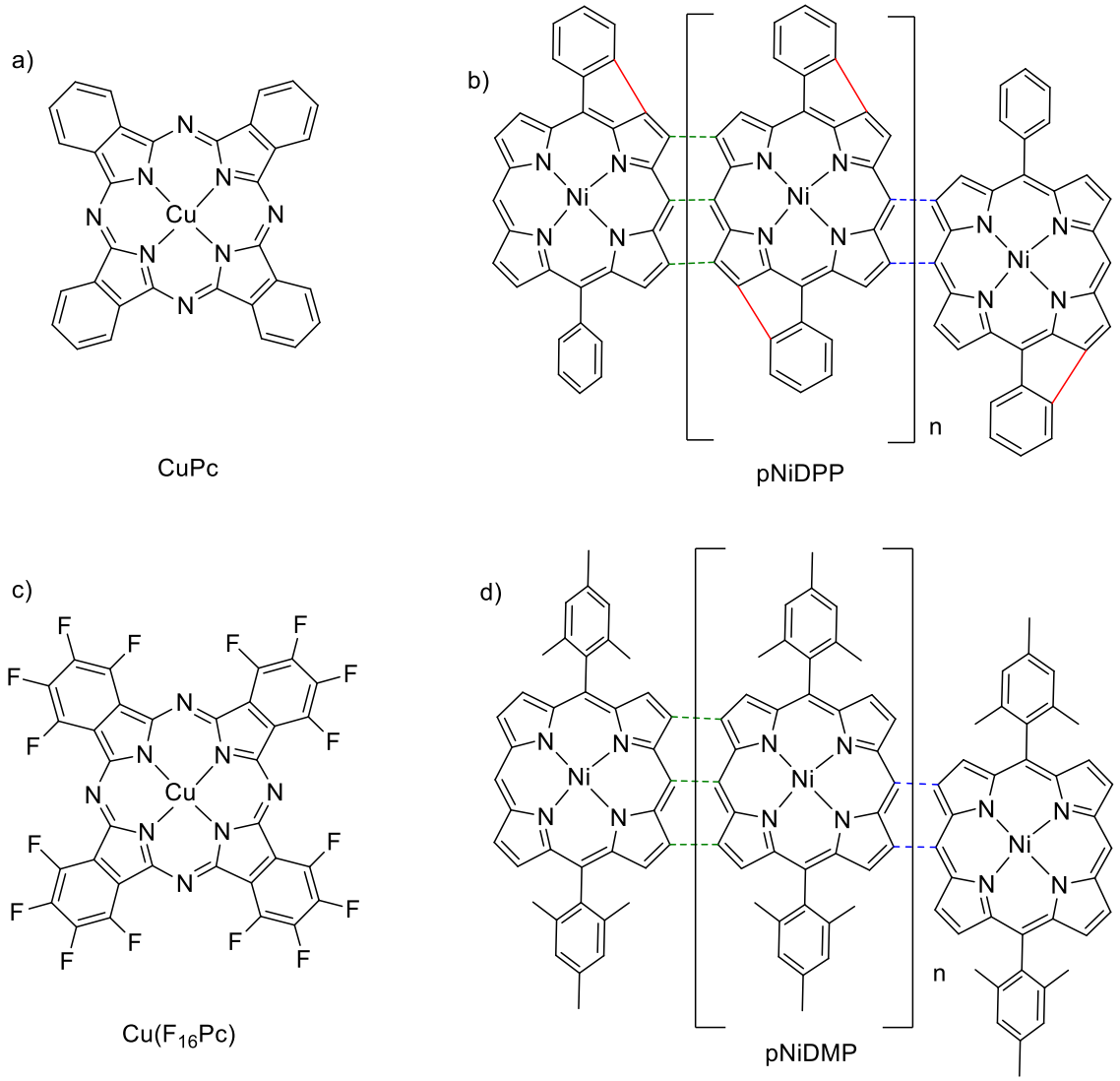

Scheme 1. Structure of a) CuPc and b) Cu(F_{16}Pc) c) pNiDPP and d) pNiDMP porphyrin tapes. The porphyrin tapes obtained from NiDPP can undergo an intramolecular dehydrogenative coupling (red line) inducing flattening of the molecular structure. From oCVD of nickel(II) porphyrins, double (blue dashed line) or triple bonds (green dashed lines) can be formed between the porphyrin units.

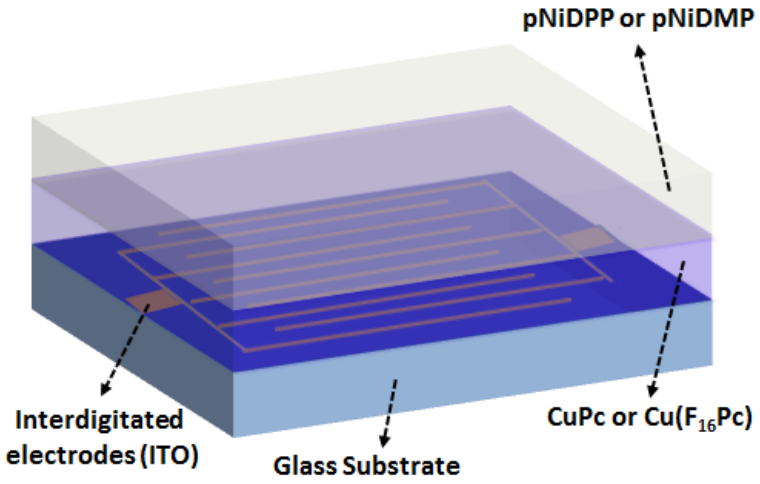

Scheme 2. Schematic of the organic heterojunction device used in this study.

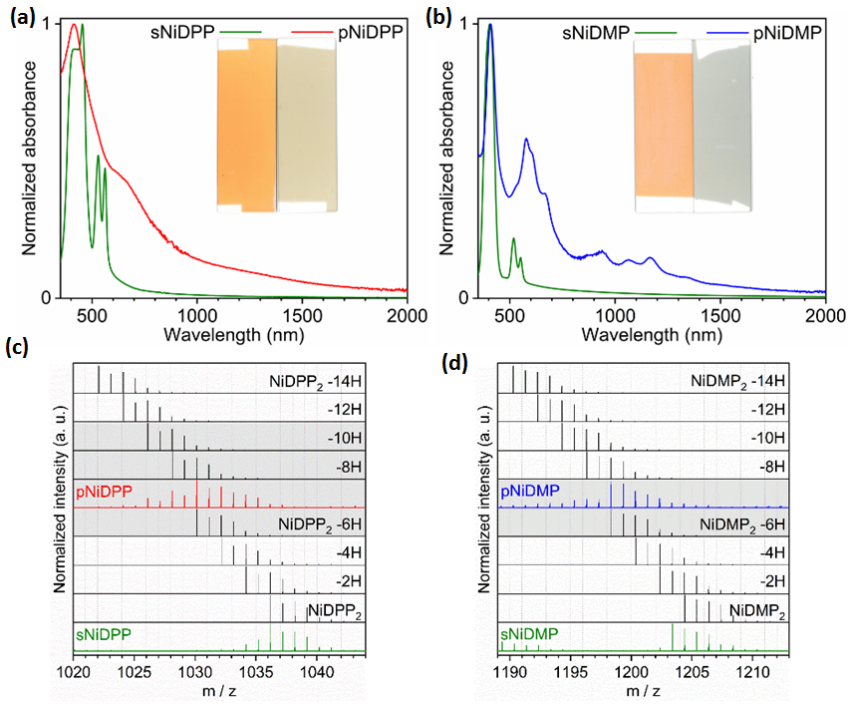

Figure 1. UV/Vis/NIR analysis of pNiDPP (a) and pNiDMP (b) films deposited on glass. A comparison to the sublimed monomers (sNiDPP and sNiDMP) and an optical image of the films is provided. LDI-HRMS analysis of pNiDPP (a) and pNiDMP (b) films dimeric region. Comparison of the spectra with the simulated patterns for different unsaturation degrees (NiDPP -xH and NiDMP -xH) is provided.

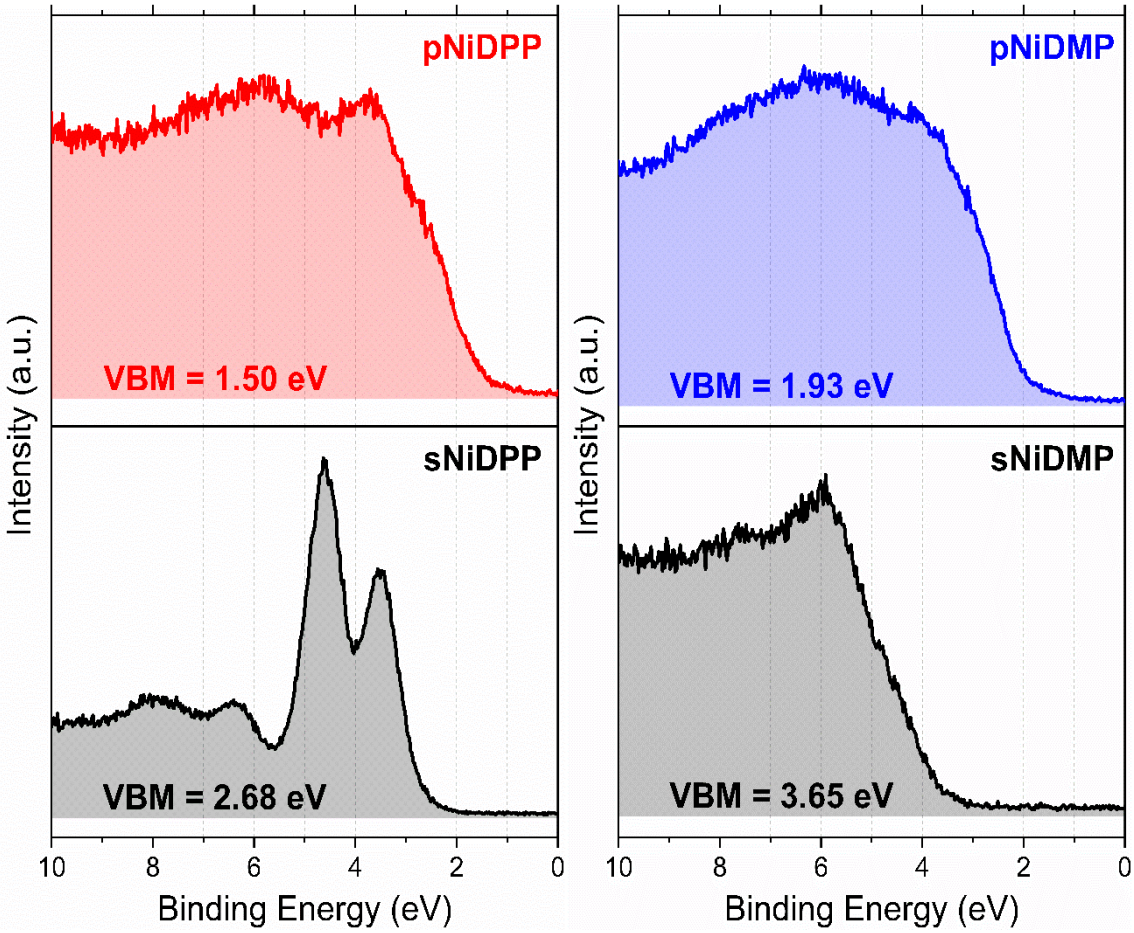

Figure 2. Valence band maxima obtained by XPS for pNiDPP, pNiDMP and their respective reference thin films, sNiDPP and sNiDMP.

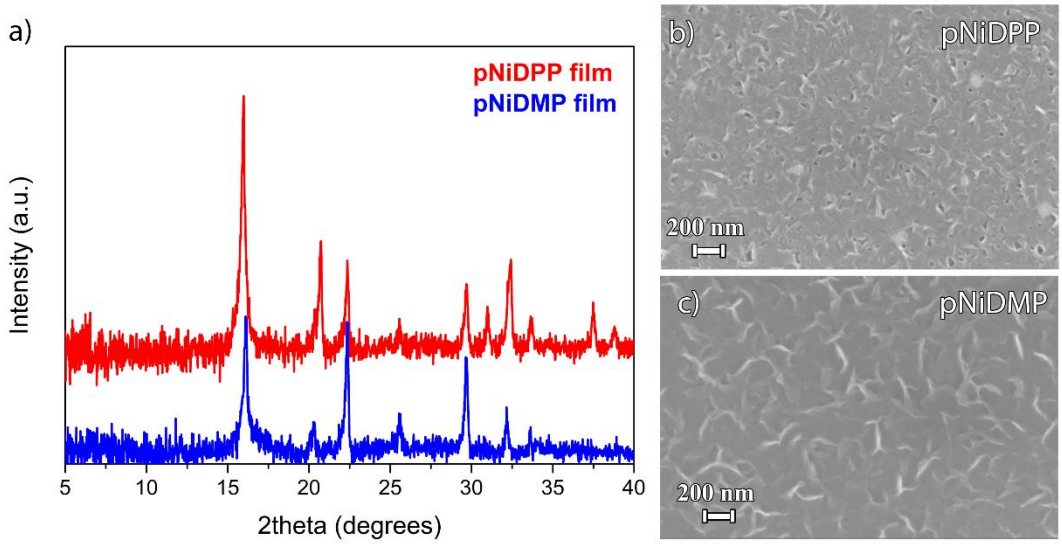

Figure 3. a) XRD patterns obtained from the analysis of pNiDMP (blue) and pNiDPP (red) films. b) FE-SEM images of pNiDPP and c) pNiDMP films at 80k magnification.

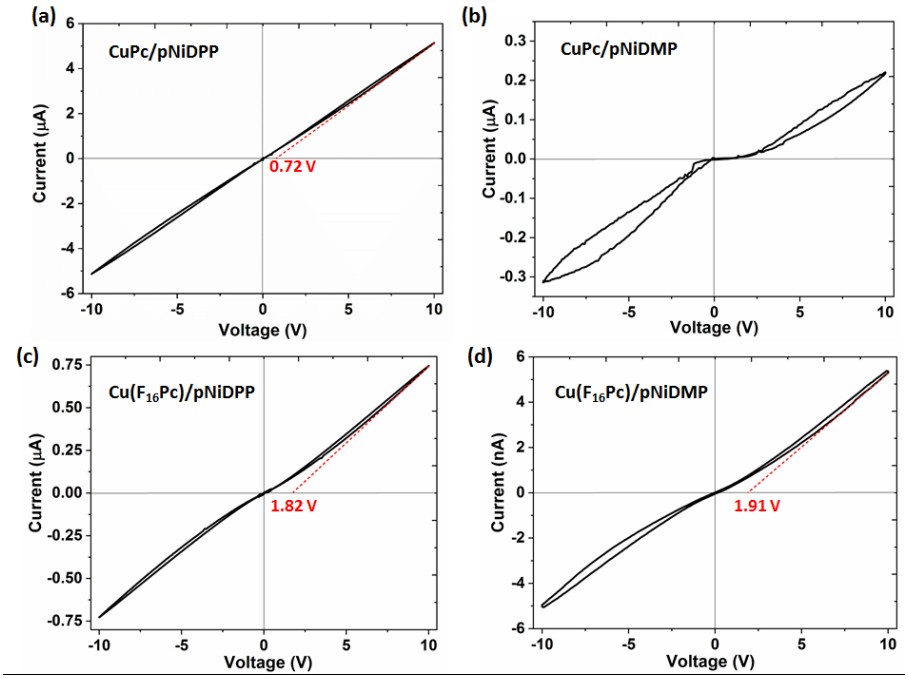

Figure 4. The I(V) curves recorded with voltage sweeps from -10 V to 10 V for CuPc/pNiDPP (a), CuPc/pNiDMP (b), Cu(F_{16}Pc)/pNiDPP (c) and Cu(F_{16}Pc)/pNiDMP device (d).

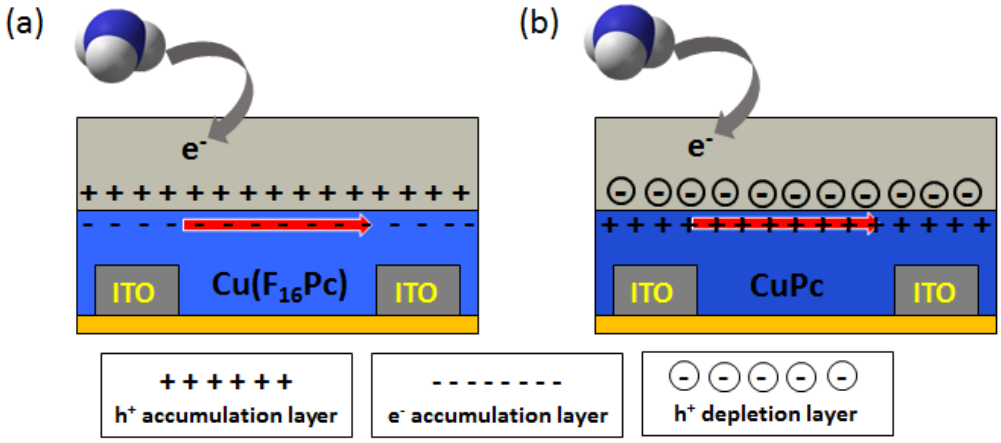

Figure 5. Representation of charges alignment at the interface of Cu(F_{16}Pc) and CuPc based devices and electron doping from ammonia exposure.

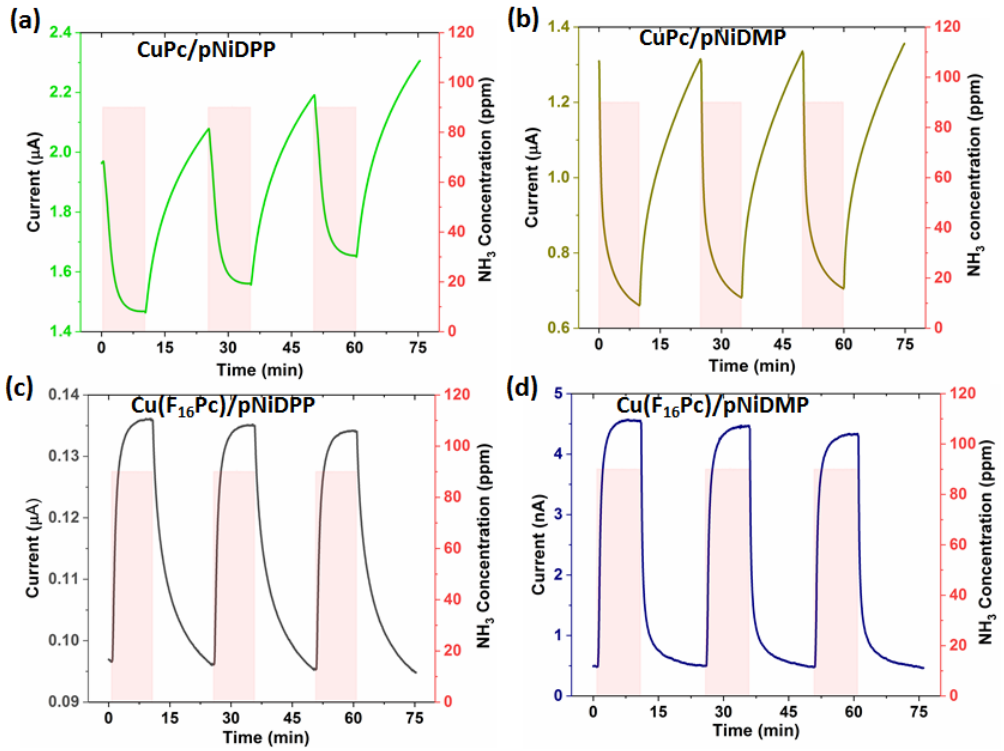

Figure 6. Typical current variation as a function of time for repeated alternate exposure periods of 90 ppm NH_3 and recovery under clean air for CuPc/pNiDPP (a), CuPc/pNiDMP (b), Cu(F_{16}Pc)/pNiDPP (c) and Cu(F_{16}Pc)/pNiDMP (d) heterojunction devices.

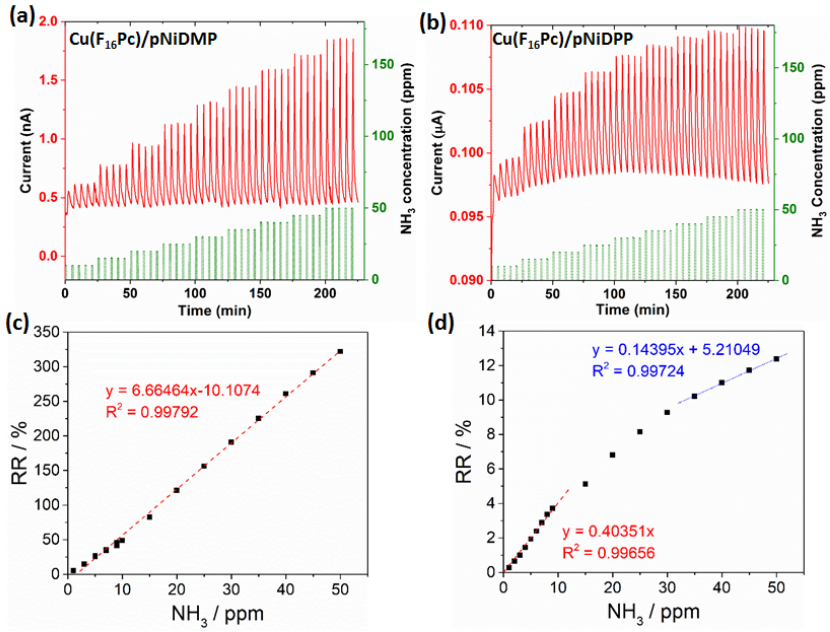

Figure 7. Current variations of Cu(F_{16}Pc)/pNiDMP (a) and Cu(F_{16}Pc)/pNiDPP (b) devices submitted to NH_3 in the range 10-50 ppm, by steps of 5 ppm, during alternate exposure/recovery cycles (1 min/4 min), at 40% rh. RR variation as a function of NH_3 concentration in 1-50 ppm range, in air, at 40 % rh, during exposure/recovery cycles (1 min/4 min) of Cu(F_{16}Pc)/pNiDMP (c) and Cu(F_{16}Pc)/pNiDPP (d) devices.

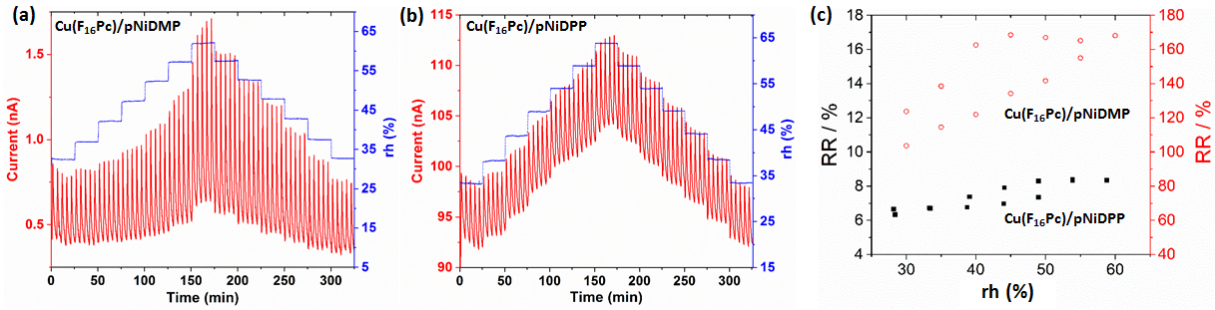

Figure 8. Current variation as a function of time for Cu(F_{16}Pc)/pNiDMP (a) and Cu(F_{16}Pc)/pNiDPP (b) devices exposed to 20 ppm NH_3, in humid air, in the range 30-60 % rh, during 1 min exposure and 4 min recovery cycles. Variations of RR with increasing and decreasing rh values for Cu(F_{16}Pc)/pNiDMP (red circle) and Cu(F_{16}Pc)/pNiDPP (black dot).

Supporting Information

Molecular Engineering of Porphyrin-Tapes/Phthalocyanine Heterojunctions for a Highly Sensitive Ammonia Sensor

Giuseppe Bengasi,[a] Rita Meunier-Prest,[b] Kamal Baba,[a] Abhishek Kumar,[b] Anna Lucia Pellegrino,[a,c] Nicolas D. Boscher,[a,] and Marcel Bouvet[b,]**

[a] *Materials Research and Technology Department, Luxembourg Institute of Science and Technology, 5, avenue des hauts-forneaux, L-4362, Esch-sur-Alzette, Luxembourg*

[b] *Institut de Chimie Moléculaire de l'Université de Bourgogne (ICMUB), UMR CNRS 6302, Université Bourgogne Franche-Comté, 9 avenue Alain Savary, 21078 Dijon cedex, France*

[c] *Dipartimento di Scienze Chimiche, Università di Catania and INSTM UdR Catania, V.le A. Doria 6, 95125 Catania, Italy*

* Corresponding author: *nicolas.boscher@list.lu*

* Corresponding author: *marcel.bouvet@u-bourgogne.fr*

Contents

Scheme S1. 32

Table S1. 33

Figure S1. 34

Scheme S2. 35

Scheme S3. 36

Table S2. 37

Figure S2. 38

Figure S3 39

Figure S4. 40

Figure S5. 41

Figure S6. 42

Figure S7 43

Table S3. 44

Table S4. 45

Figure S8. 46

Figure S9. 46

Figure S10. 47

Table S5. 48

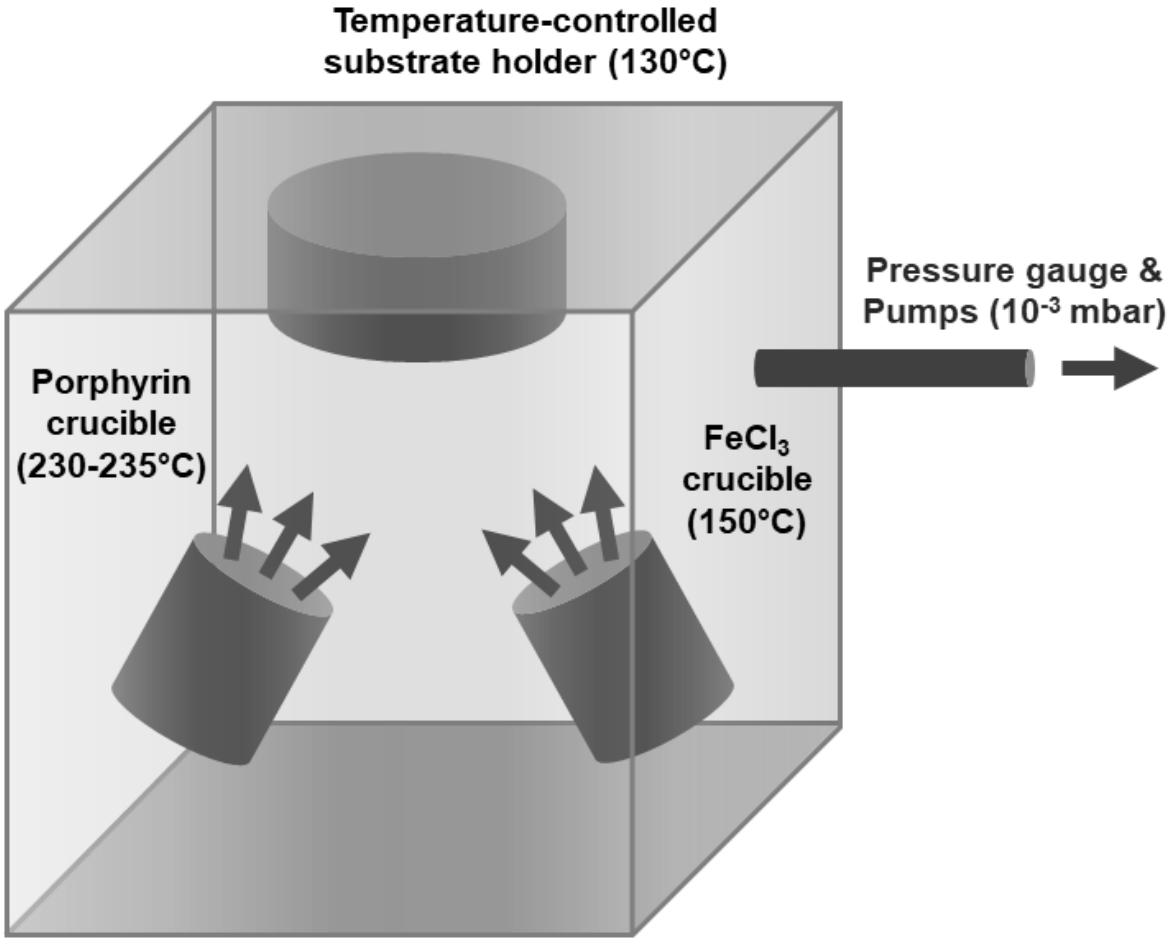

Scheme S1. Oxidative chemical vapour deposition (oCVD) reactor used for the preparation of the pNiDPP and pNiDMP thin films and CuPc/pNiDPP, Cu(F_{16}Pc)/pNiDPP, CuPc/pNiDMP and Cu(F_{16}Pc)/pNiDMP devices. The nickel(II) porphyrins (NiDPP and NiDMP) and the oxidant ($FeCl_3$) were simultaneously sublimed under reduced pressure (10^{-3} mbar) using two crucibles located in the lower part of the chamber. The crucible temperatures were set to 235°C, 230°C and 150°C for NiDPP, NiDMP and $FeCl_3$, respectively. The substrates were placed on a heated stage (130°C) placed 20 cm above the two crucibles. The reference sNiDPP and sNiDMP thin films were prepared by sublimation using the same chamber without $FeCl_3$.

Table S1. Chemical vapor deposition reaction conditions for the preparation of the fused porphyrin thin films (pNiDPP and pNiDMP), heterojunction devices (CuPc/pNiDPP, Cu(F_{16}Pc)/pNiDPP, CuPc/pNiDMP and Cu(F_{16}Pc)/pNiDMP) and reference porphyrin thin films (sNiDPP and sNiDMP).

	sNiDPP	**pNiDPP**	**pNiDMP**	**sNiDMP**
Monomer	Nickel(II) 5,15-(diphenyl)porphyrin		Nickel(II) 5,15-(dimesityl)porphyrin	
Chemical formula	$C_{32}H_{20}N_4Ni$		$C_{38}H_{32}N_4Ni$	
Molecular weight	518.104143 g·mol^{-1}		602.198043 g·mol^{-1}	
Sublimation temperature	235 °C		230 °C	
Sublimed amount	3.9 mg 7.5 µmol		5.4 mg 9.0 µmol	
Oxidant	N/A	Iron Chloride		N/A
Chemical formula		$FeCl_3$		
Molecular weight		160.841498 g·mol^{-1}		
Sublimation temperature		150°C		
Sublimed amount		50.6 mg 314.6 µmol		
Pressure	10^{-3} mbar			
Substrate temperature	130 °C			
Deposition time	5 minutes			

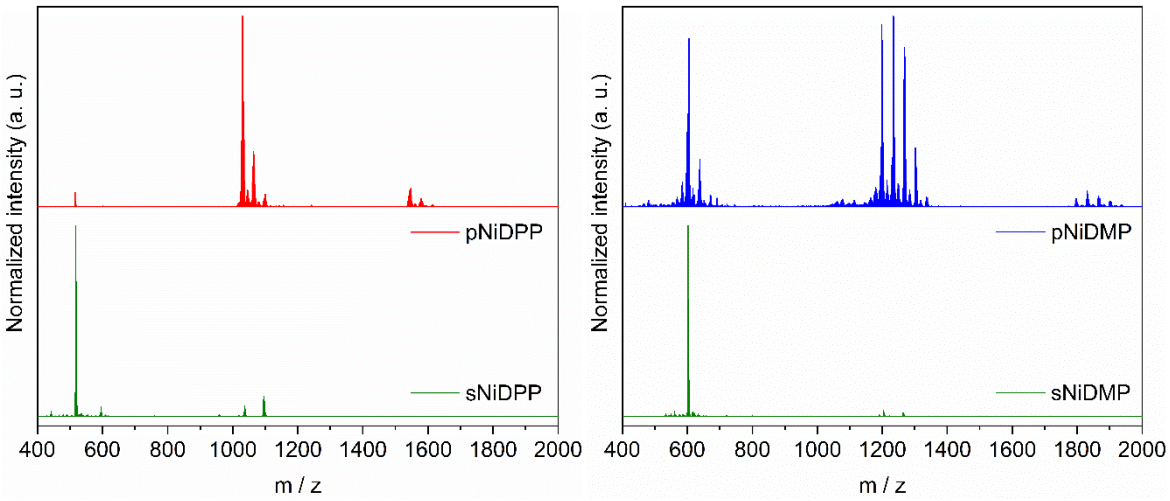

Figure S1. Laser desorption ionization high-resolution mass spectrometry (LDI-HRMS) of the (a) pNiDPP and reference sNiDPP thin films and (b) pNiDMP and reference sNiDMP thin films. The spectra of the pNiDPP and pNiDMP reveal the presence of oligomeric species and peak distributions related to the exchange of hydrogen by chlorine atoms deriving from the oxidant.

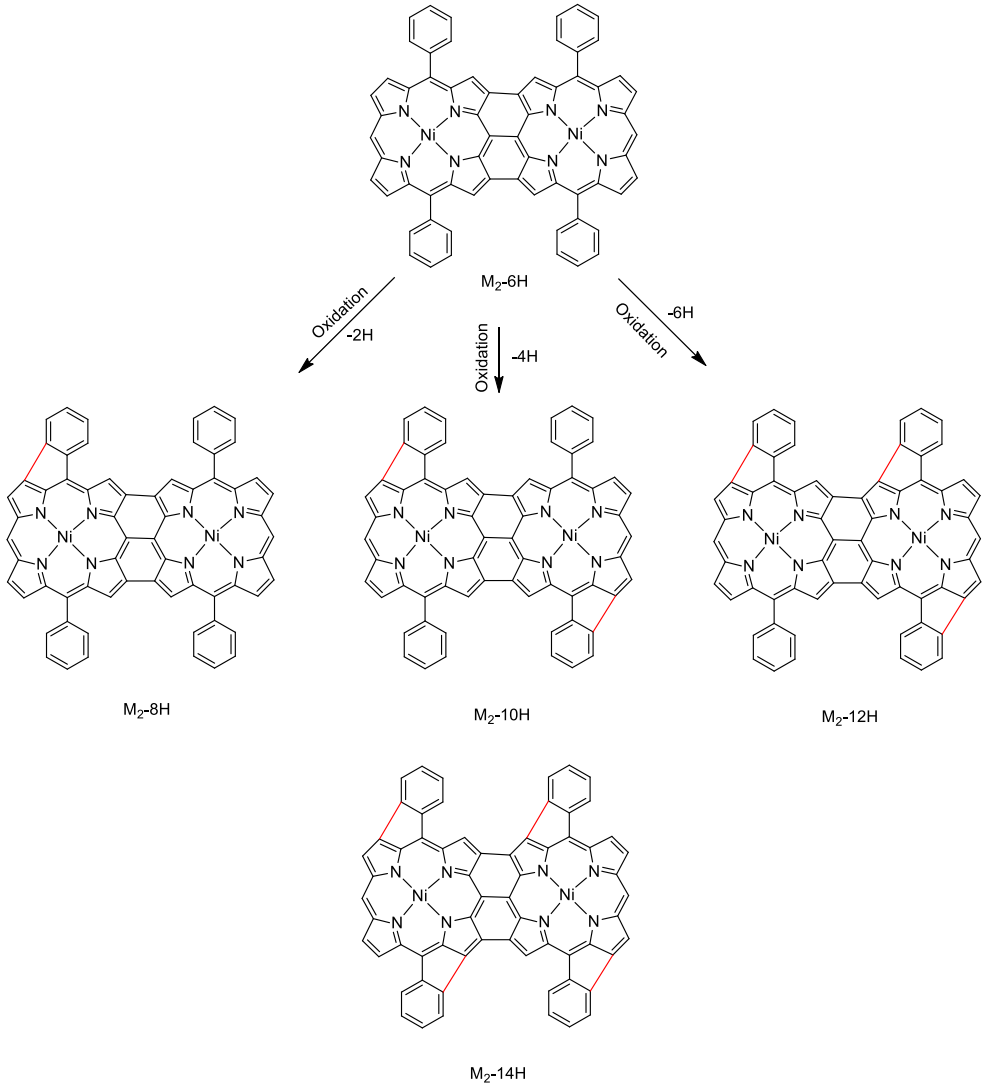

Scheme S2. Schematic of the detected dimeric triply linked NiDPP species formed during the oCVD reaction of NiDPP.

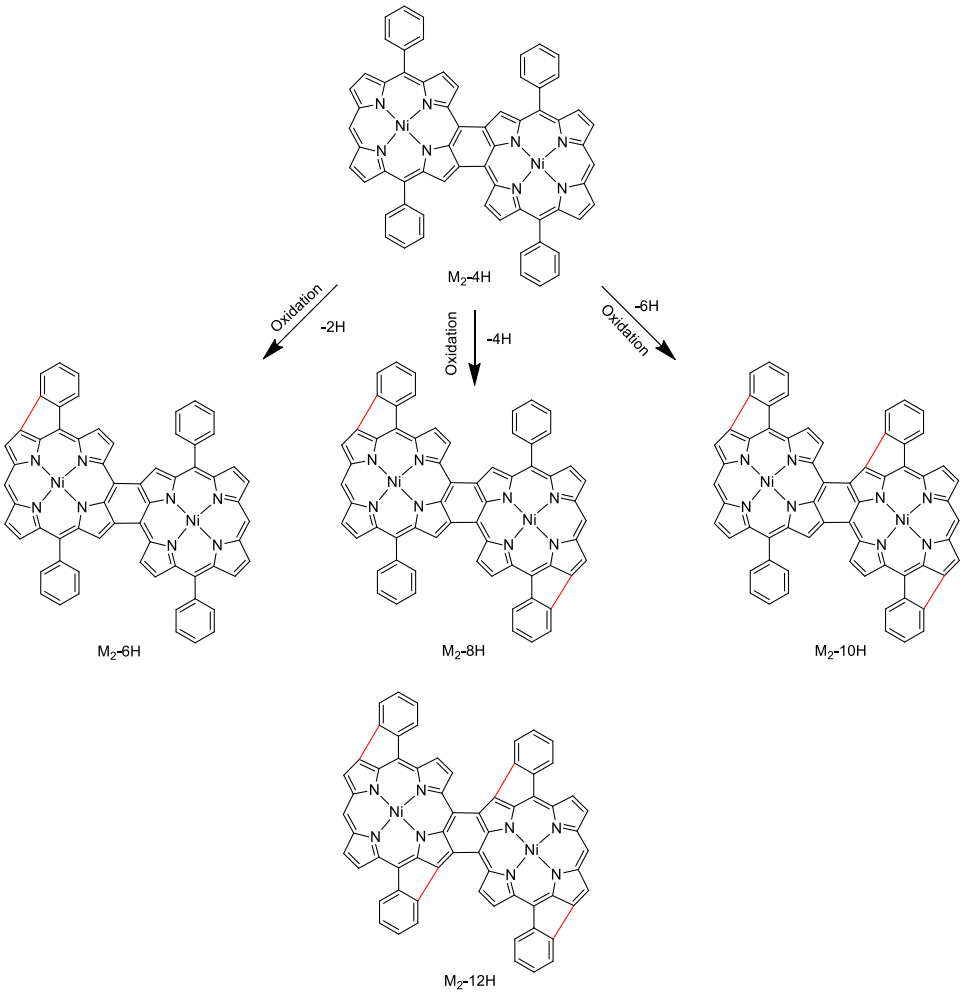

Scheme S3. Schematic of the detected dimeric doubly linked NiDPP species formed during the oCVD reaction of NiDPP.

Table S2. Relative atomic concentration by XPS of the pNiDPP, sNiDPP, pNiDMP and sNiDMP thin films and theoretical composition of NiDPP and NiDMP.

	Ni (%)	**N (%)**	**C (%)**	**Cl (%)**	**Fe (%)**
NiDPP (theo.)	2.7	10.8	86.5	-	-
sNiDPP (exp.)	2.7	10.8	86.5	0.0	0.0
pNiDPP (exp.)	1.6	5.7	88.2	2.7	1.8
NiDMP (theo.)	2.3	9.3	88.4	-	-
sNiDMP (exp.)	2.1	9.3	88.6	0.0	0.0
pNiDMP (exp.)	1.4	5.8	87.9	2.7	2.2

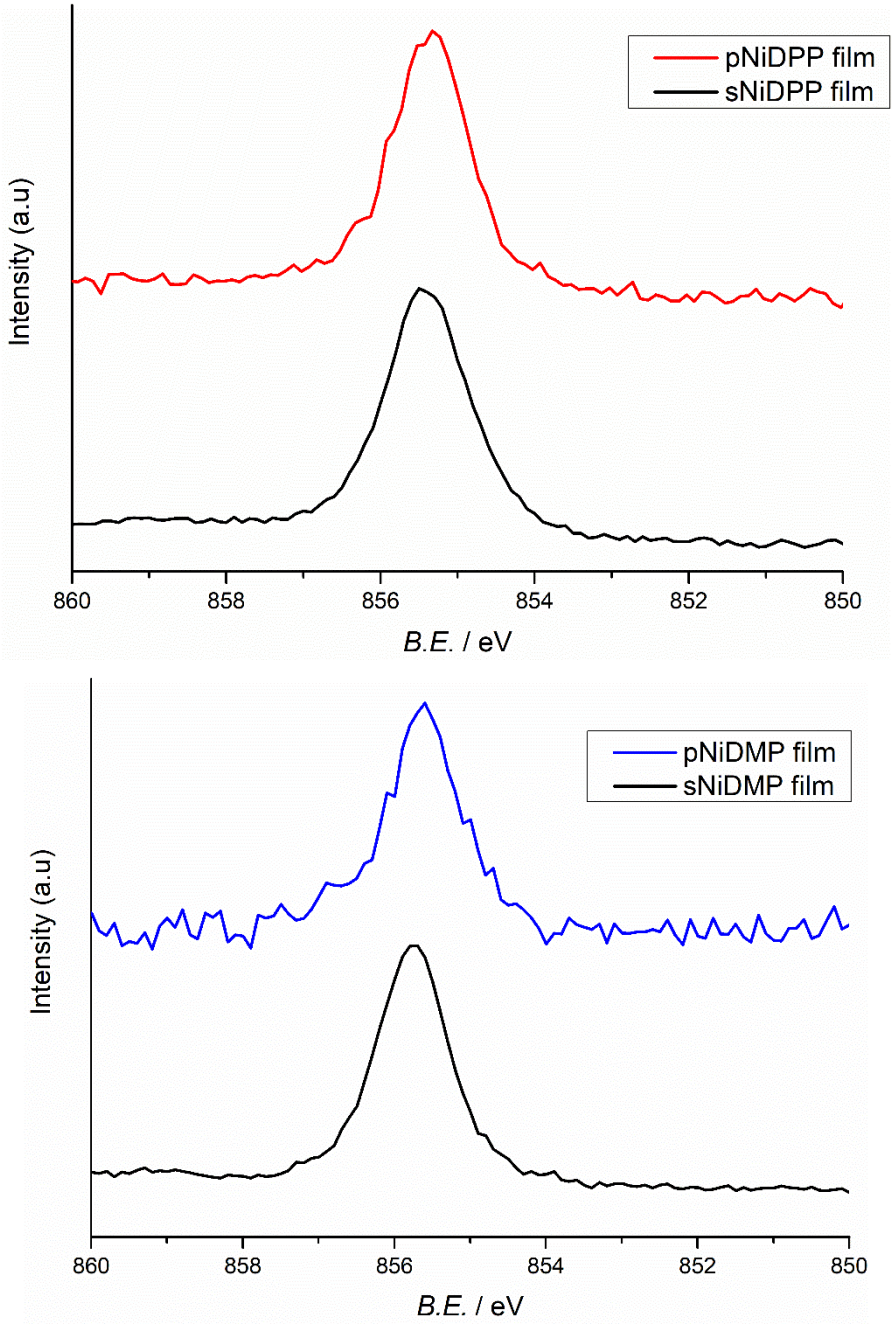

Figure S2. XPS spectra in the Ni 2p region for the pNiDPP, pNiDMP films and respective reference of the sublimed monomers.

pNiDPP

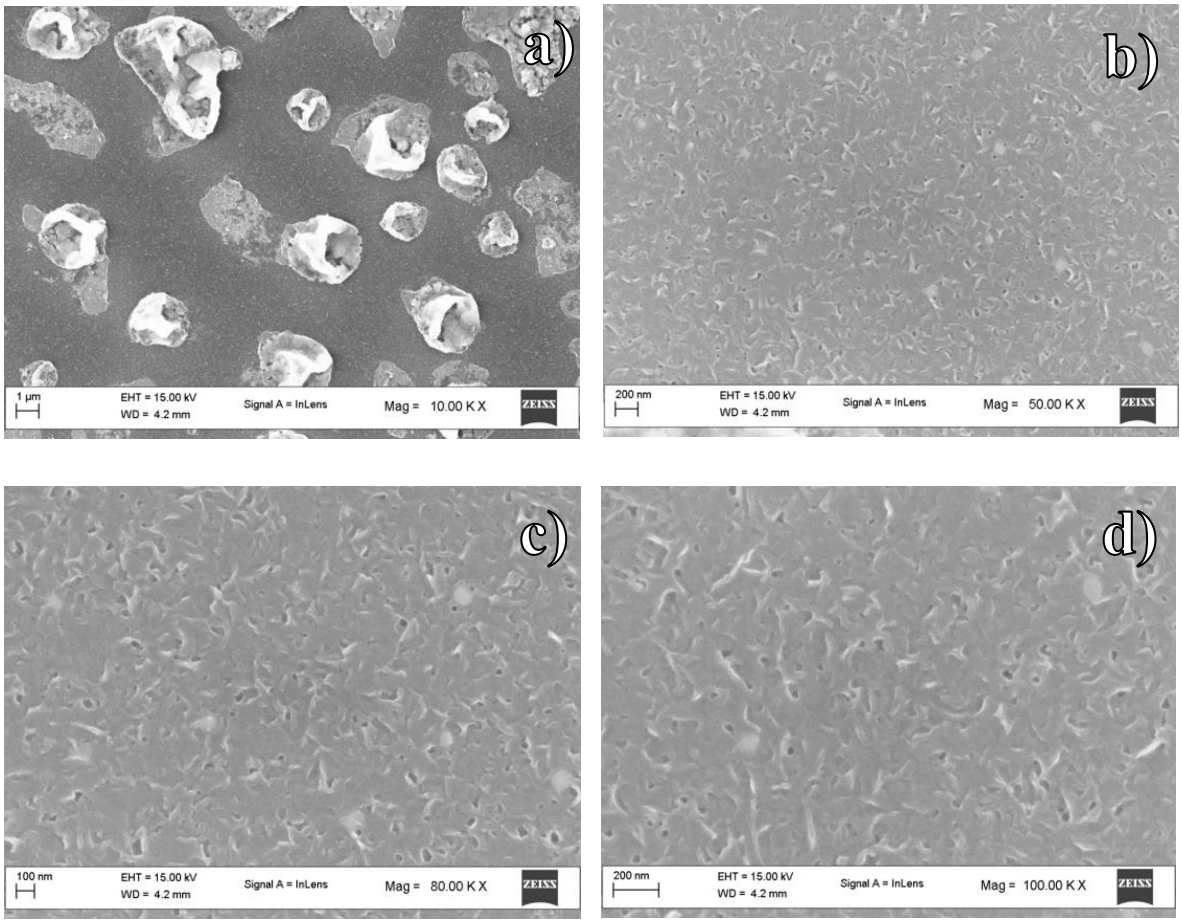

Figure S3. FE-SEM images of the pNiDPP thin film at different magnification a) 10’000, b) 50’000, c) 80’000, d) 100’000. Lower magnification highlight the presence of iron chloride residues and a more porous structure of the film compared to pNiDMP.

pNiDMP

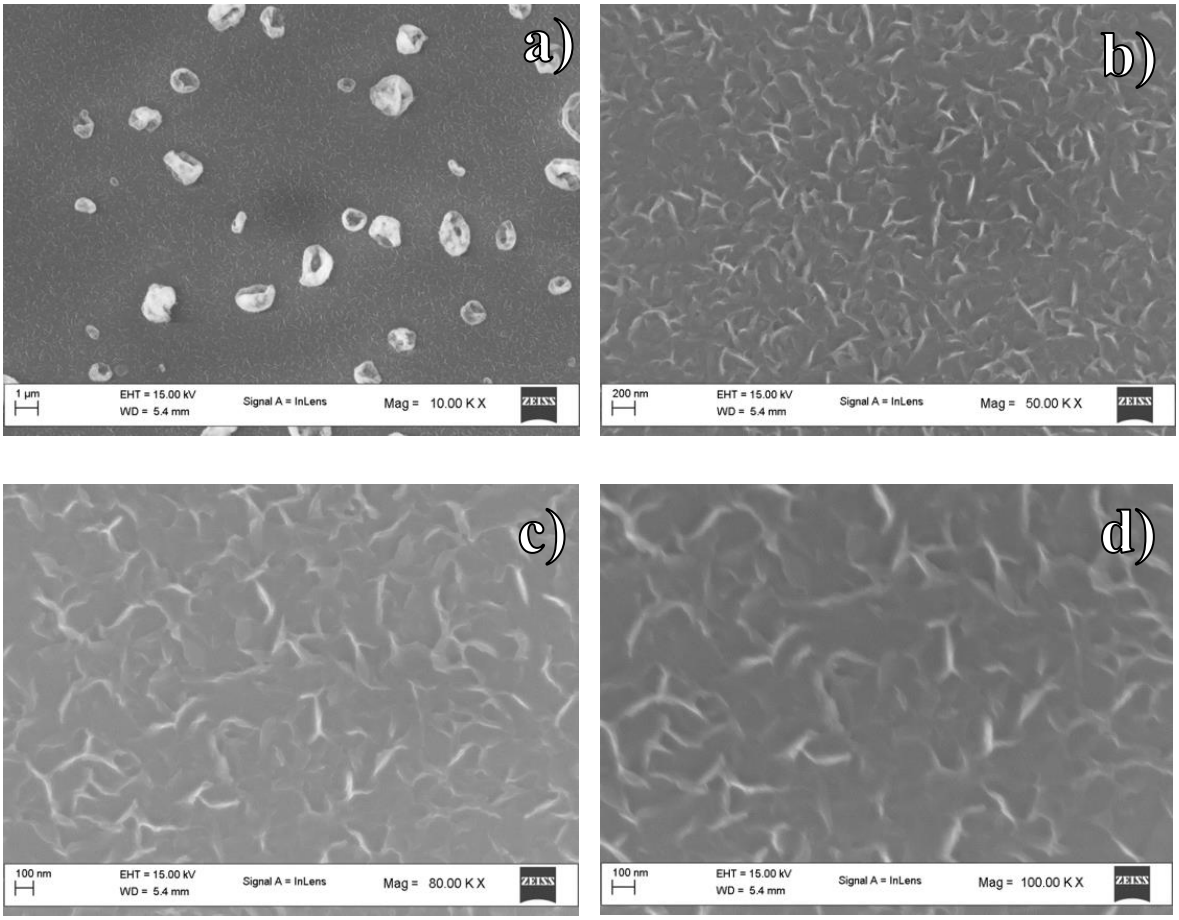

Figure S4. FE-SEM images of the pNiDMP thin film at different magnification a) 10’000, b) 50’000, c) 80’000, d) 100’000. Lower magnification highlight the presence of iron chloride residues and a more compact structure compared to pNiDPP.

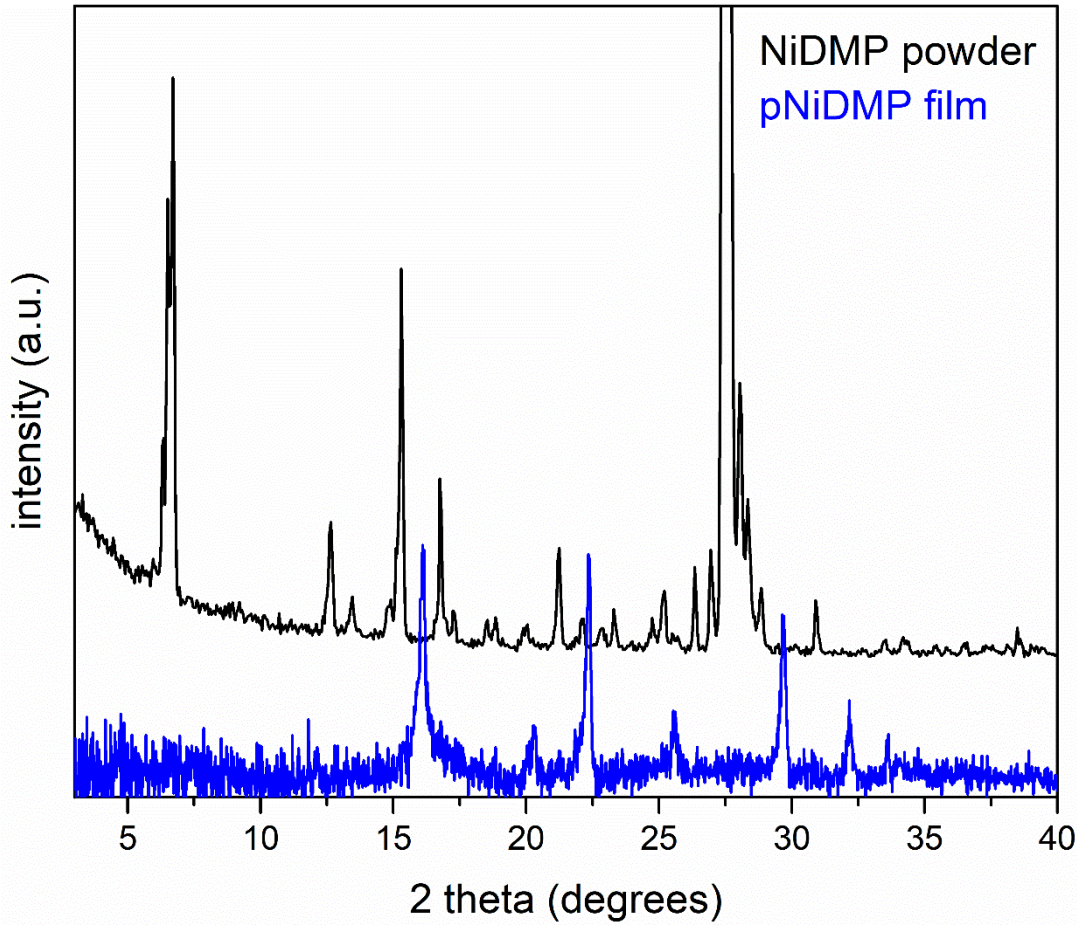

Figure S5. Comparison between the XRD patterns of the NiDMP monomer powder (black) and pNiDMP thin film (blue).

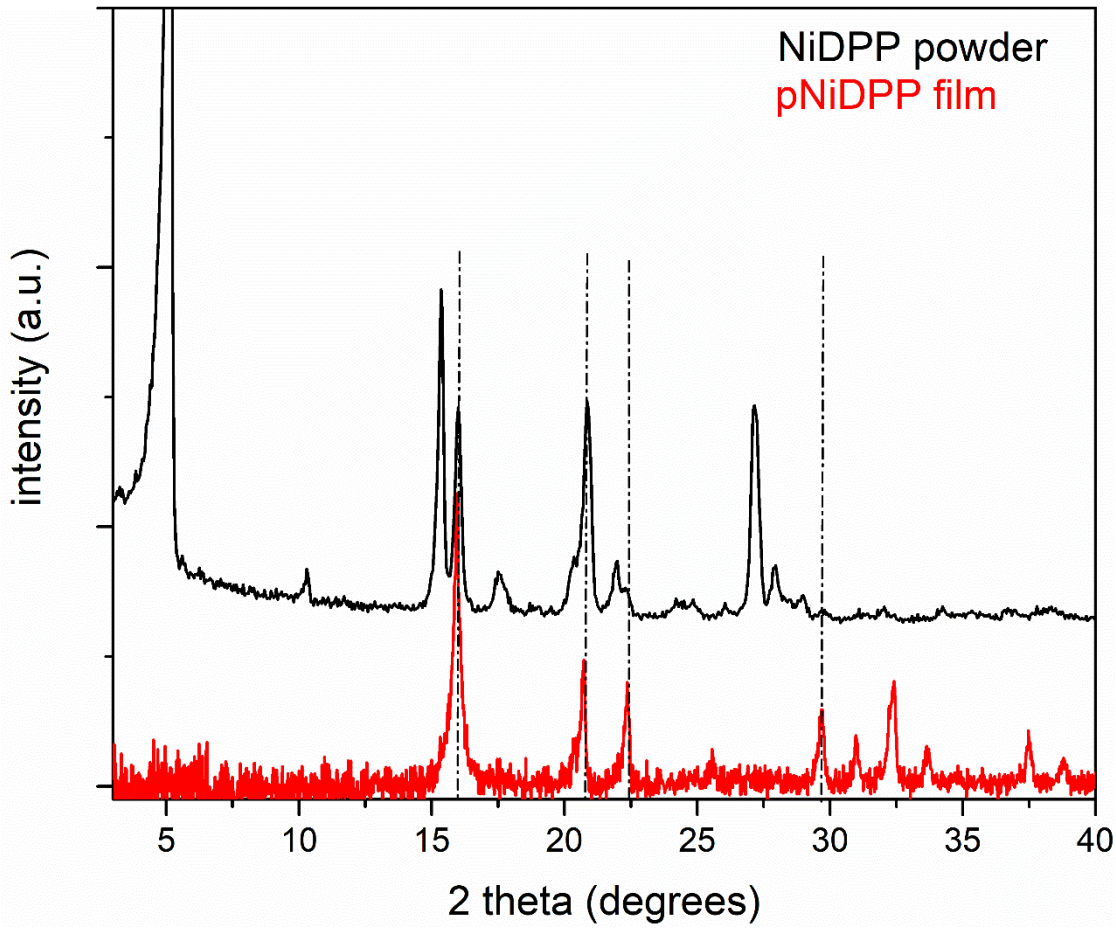

Figure S6. Comparison between the XRD patterns of the NiDPP monomer powder (black) and pNiDPP thin film (red).

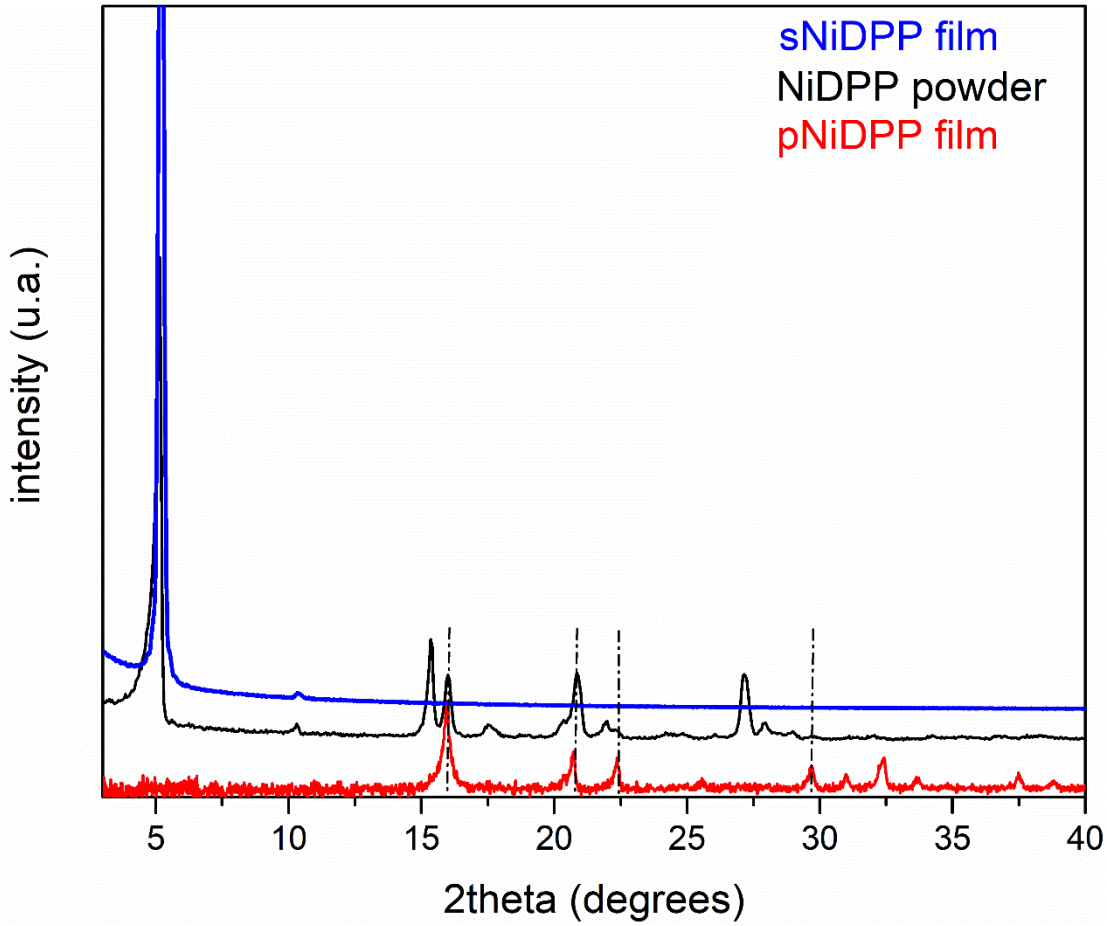

Figure S7. Comparison between the XRD patterns of sublimed NiDPP film (sNiDPP, blue), NiDPP powder (black) and pNiDPP film (red).

Table S3. List and identification of the peaks observed by XRD for the pNiDPP and pNiDMP thin films.

XRD PEAKS' ANALYSIS				
pNiDPP *2 theta*	**pNiDMP** *2 theta*	**Reflection order**	**hkl**	***d* / Å**
15.96°		n: 1	010	5.54(6)
	16.11°	n:1	010	5.49(5)
	20.30°			4.36(9)
20.70°				4.28(6)
22.35°	22.35°			3.97(3)
25.58°	25.58°			3.47(8)
29.68°	29.68°			3.00(6)
31.00°				2.88(1)
	32.16°	or n: 2	020	2.77(9) 5.55(9)
32.37°		or n: 2	020	2.76(2) 5.52(4)
33.68°				2.65(7)
37.48°				2.39(6)
38.80°				2.31(8)

Table S4. Relative response, response time and recovery time of the studied heterojunction devices.

Sensors	**Relative Response (%)**	**Response time (min)**	**Recovery time (min)**
CuPc/pNiDPP	-24.5	3.9	12.0
CuPc/pNiDMP	-48.0	4.3	12.1
Cu(F_{16}Pc)/pNiDPP	40.5	2.7	9.2
Cu(F_{16}Pc)/pNiDMP	788	2.2	2.8

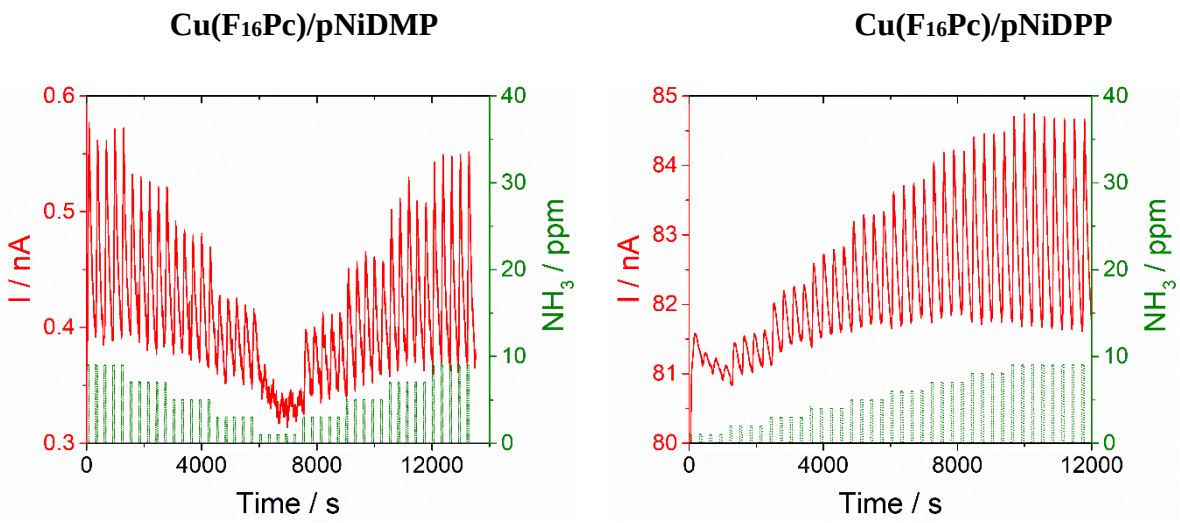

Figure S8. Response of Cu(F_{16}Pc)/pNiDMP (left, at a bias of 2 V) and Cu(F_{16}Pc)/pNiDPP (right, at a bias of 5 V, to NH_3, in the range 1-9 ppm, during exposure/recovery cycles (1 min / 4 min), at 40 % RH.

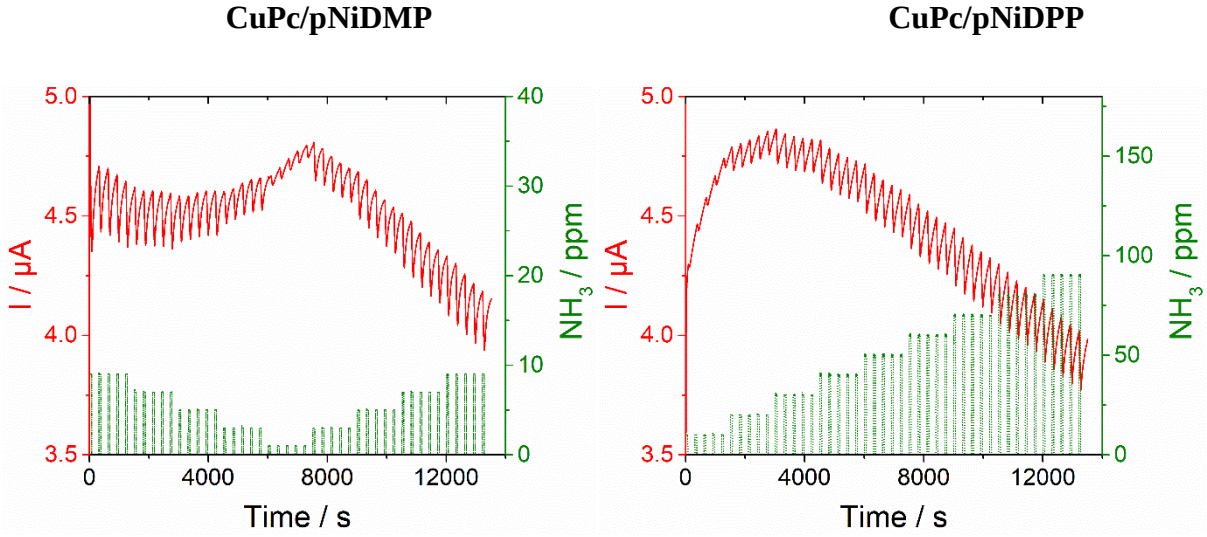

Figure S9. Response to NH_3 of CuPc/pNiDMP in the 10-50 ppm range (left) and of CuPc/pNiDPP in the 1-9 ppm range (right), showing the fluctuation of the baseline, during exposure/recovery cycles (1 min / 4 min), at 40 % RH, both at a bias of 2 V.

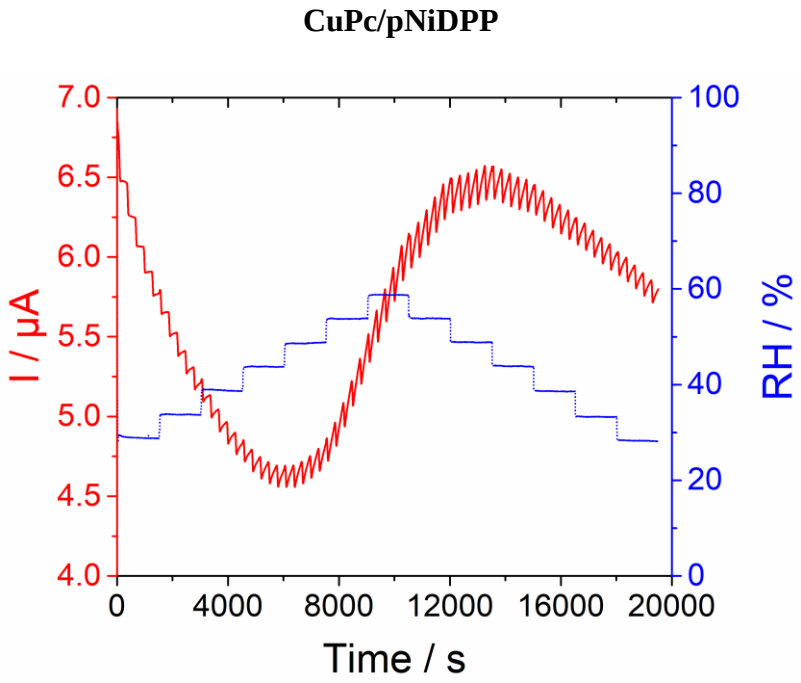

Figure S10. Current as a function of time of a CuPc/pNiDPP heterojunction exposed to 20 ppm NH3, in humid air, in the range 30-60 % RH, during exposure/recovery cycles (1 min / 4 min).

Table S5. Summary of the sensing properties of the present devices compared to the literature.[37–41,48–54]

Devices	RR [%]	$[NH_3]$ [ppm]	S [% ppm^{-1}]	LOD [ppb]	$[NH_3]$ [ppm]	T [°C]	rh [%]	Ref.
Cu(F_{16}Pc)/pNiDPP heterojunction	40	90	0.4	228	1-9	25	40	This work
Cu(F_{16}Pc)/pNiDMP heterojunction	788	90	6.7	1000	1-50	25	40	This work
Co(Cl_8Pc)/$LuPc_2$ heterojunction	58	90	1.48	250	1-9	25	30	1
Cu(Cl_8Pc)/$LuPc_2$ heterojunction	55	90	0.14	1200	1-9	25	30	1
Cu(F_{16}Pc)/$LuPc_2$ heterojunction	67	90	1.5	280	1 - 9	25	50	2
DMBz/Cu(F_{16}Pc)/$LuPc_2$ heterojunction	138	90	3	140	1 - 9	25	50	2
TFBz/Cu(F_{16}Pc) – $LuPc_2$ heterojunction	50	90	1.1	2000	1 - 9	25	50	2
PTCDI/$LuPc_2$ heterojunction	34	90	0.6		10 - 30	25	50	3
TPDO/Lu Pc_2 heterojunction	26	90	0.2		30 - 90	25	50	4
PTFA/$LuPc_2$ heterojunction	14	90	1.05	450	1 - 6	25	50	5
PDMA/$LuPc_2$ heterojunction	14	90	2.23	314	1 - 6	25	50	6
PANI/CuTsPc chemiresistor	78	30	1.9		10 - 30	25	50	7
PPy chemiresistor	16	40	0.2	1000	40-75	25		8
PEDOT/PSS-SWCNT chemiresistor	33	300	0.21	200	2 - 100			9
CVD synthesized graphene chemiresistor	40	40	6 – 0.09*	≈ 500	0.5 – 1000*	25**		10
MoO_3-WO_3 chemiresistor	1000	5	200		5			11
CeO_2 – PANI chemiresistor	550	50	11		2 - 50			12

* non-linear but measured down to 0.5 ppm; ** measured at 25°C but desorption was achieved by heating under vacuum at ca. 200°C

References

[1] S. Ouedraogo, R. Meunier-Prest, A. Kumar, M. Bayo-Bangoura, M. Bouvet, *ACS Sensors*, **2020**, *5*, 1849–1857.

[2] M. Mateos, R. Meunier-Prest, J. M. Suisse, M. Bouvet, *Sensors Actuators, B Chem.*, **2019**, *299*, 126968.

[3] P. Gaudillat, A. Wannebroucq, J. M. Suisse, M. Bouvet, *Sensors Actuators, B Chem.*, **2016**, *222*, 910–917.

[4] A. Wannebroucq, G. Gruntz, J.-M. Suisse, Y. Nicolas, R. Meunier-Prest, M. Mateos, T. Toupance, M. Bouvet, *Sensors Actuators B Chem.*, **2018**, *255*, 1694–1700.

[5] M. Mateos, R. Meunier-Prest, O. Heintz, F. Herbst, J. M. Suisse, M. Bouvet, *ACS Appl. Mater. Interfaces*, **2018**, *10*, 19974–19986.

[6] M. Mateos, M.-D. Tchangaï, R. Meunier-Prest, O. Heintz, F. Herbst, J.-M. Suisse, M. Bouvet, *ACS Sensors*, **2019**, *4*, 740–747.

[7] P. Gaudillat, F. Jurin, B. Lakard, C. Buron, J.-M. Suisse, M. Bouvet, *Sensors*, **2014**, *14*, 13476–13495.

[8] T. Patois, J.-B. Sanchez, F. Berger, J.-Y. Rauch, P. Fievet, B. Lakard, *Sensors Actuators B Chem.*, **2012**, *171–172*, 431–439.

[9] J. Jian, X. Guo, L. Lin, Q. Cai, J. Cheng, J. Li, *Sensors Actuators, B Chem.*, **2013**, *178*, 279–288.

[10] F. Yavari, E. Castillo, H. Gullapalli, P. M. Ajayan, N. Koratkar, *Appl. Phys. Lett.*, **2012**, *100*, 203120.

[11] C. . Xu, N. Miura, Y. Ishida, K. Matsuda, N. Yamazoe, *Sensors Actuators B Chem.*, **2000**, *65*, 163–165.

[12] L. Wang, H. Huang, S. Xiao, D. Cai, Y. Liu, B. Liu, D. Wang, C. Wang, H. Li, Y. Wang, Q. Li, T. Wang, *ACS Appl. Mater. Interfaces*, **2014**, *6*, 14131–14140.